

High-resolution CARMA Observation of Molecular Gas in the North America and Pelican Nebulae

SHUO KONG,^{1,2} HÉCTOR G. ARCE,² JOHN M. CARPENTER,³ JOHN BALLY,⁴ VOLKER OSSENKOPF-OKADA,⁵
ÁLVARO SÁNCHEZ-MONGE,⁵ ANNEILA I. SARGENT,⁶ SÜMEYYE SURI,⁷ PEREGRINE MCGEHEE,⁸ DARIUSZ C. LIS,⁹
RALF KLESSEN,^{10,11} STEVE MAIRS,¹² CATHERINE ZUCKER,¹³ ROWAN J. SMITH,¹⁴ FUMITAKA NAKAMURA,¹⁵
THUSHARA G.S. PILLAI,¹⁶ JENS KAUFFMANN,¹⁷ AND SHAOBO ZHANG¹⁸

¹*Steward Observatory, University of Arizona, Tucson, AZ 85719, USA*

²*Department of Astronomy, Yale University, New Haven, CT 06511, USA*

³*Joint ALMA Observatory, Avenida Alonso de Córdova 3107, Vitacura, Santiago, Chile*

⁴*Department of Astrophysical and Planetary Sciences, University of Colorado, Boulder, Colorado, USA*

⁵*I. Physikalisches Institut, Universität zu Köln, Zùlpicher Str. 77, D-50937 Köln, Germany*

⁶*Division of Physics, Mathematics and Astronomy, California Institute of Technology 249-17, Pasadena, CA 91125, USA*

⁷*Max Planck Institute for Astronomy, Königstuhl 17, 69117 Heidelberg, Germany*

⁸*Department of Earth and Space Sciences, College of the Canyons, Santa Clarita, CA 91355*

⁹*Jet Propulsion Laboratory, California Institute of Technology, 4800 Oak Grove Drive, Pasadena, CA 91109, USA*

¹⁰*Universität Heidelberg, Zentrum für Astronomie, Albert-Ueberle-Str. 2, 69120 Heidelberg, Germany*

¹¹*Universität Heidelberg, Interdisziplinäres Zentrum für Wissenschaftliches Rechnen, INF 205, 69120 Heidelberg, Germany*

¹²*East Asian Observatory, 660 N. A'ohōkū Place, Hilo, Hawai'i, 96720, USA*

¹³*Harvard Astronomy, Harvard-Smithsonian Center for Astrophysics, 60 Garden St., Cambridge, MA 02138, USA*

¹⁴*Jodrell Bank Centre for Astrophysics, Department of Physics and Astronomy, University of Manchester, Oxford Road, Manchester M13 9PL, UK*

¹⁵*National Astronomical Observatory of Japan, 2-21-1 Osawa, Mitaka, Tokyo 181-8588, Japan*

¹⁶*Institute for Astrophysical Research, Boston University, Boston, MA, USA.*

¹⁷*Haystack Observatory, Massachusetts Institute of Technology, 99 Millstone Road, Westford, MA 01886, USA*

¹⁸*Purple Mountain Observatory, & Key Laboratory for Radio Astronomy, Chinese Academy of Sciences, Nanjing 210023, China*

ABSTRACT

We present the first results from a CARMA high-resolution ¹²CO(1-0), ¹³CO(1-0), and C¹⁸O(1-0) molecular line survey of the North America and Pelican (NAP) Nebulae. CARMA observations have been combined with single-dish data from the Purple Mountain 13.7m telescope to add short spacings and produce high-dynamic-range images. We find that the molecular gas is predominantly shaped by the W80 HII bubble that is driven by an O star. Several bright rims are probably remnant molecular clouds heated and stripped by the massive star. Matching these rims in molecular lines and optical images, we construct a model of the three-dimensional structure of the NAP complex. Two groups of molecular clumps/filaments are on the near side of the bubble, one being pushed toward us, whereas the other is moving toward the bubble. Another group is on the far side of the bubble and moving away. The young stellar objects in the Gulf region reside in three different clusters, each hosted by a cloud from one of the three molecular clump groups. Although all gas content in the NAP is impacted by feedback from the central O star, some regions show no signs of star formation, while other areas clearly exhibit star formation activity. Other molecular gas being carved by feedback includes the cometary structures in the Pelican Head region and the boomerang features at the boundary of the Gulf region. The results show that the NAP complex is an ideal place for the study of feedback effects on star formation.

1. INTRODUCTION

Feedback from young massive stars is crucial for the evolution of the interstellar medium of galaxies. In particular, bubbles driven by young massive stars are common in our Milky Way (Churchwell et al. 2006). They carry momentum and energy and significantly impact their environments. However, details of these regulatory

processes are not well understood, largely because the structure of the gas is often complicated by the effects of multiple massive stars (Dale et al. 2015). Studies of the effects of a single massive star on its natal molecular environment are clearly needed to address this issue.

In this regard, the North America and Pelican (NAP) Nebulae provide a favorable target for investigating the response of a star-forming molecular cloud to a single

massive star and its feedback. Within this complex, an HII region, W80, appears as an ionized bubble at radio wavelengths (Westerhout 1958). The ionizing source is an O3.5 star, 2MASS J20555125+4352246 (Comerón & Pasquali 2005), also known as the Bajamar Star (with the possibility of being a spectroscopic binary, Maíz Apellániz et al. 2016).

An optical/near infrared image of the NAP is shown in Figure 1. A dark cloud, L935, is seen against the bright W80 bubble. The position of the Bajamar Star is indicated by a cyan diamond. The HII region has been produced by a single massive ionizing source still embedded in an actively star-forming molecular cloud (Bally et al. 2014, hereafter B14). This is an ideal area for a detailed study of the effects of massive star feedback on the surrounding environment.

Based on the recent Gaia data, we have learned that the NAP region is about 800 pc away (Zucker et al. 2020, also see §4.3). At this distance, a physical scale of 0.1 pc translates to an angular scale of 25". The scale corresponds to the typical size of star-forming cores and filaments, which are most relevant to star formation studies. To reasonably resolve these structures in the NAP cloud, we have used the Combined Array for Research in Millimeter-wave Astronomy (CARMA) to map emission from common molecular gas tracers (§2.1). The NAP complex is vast, so we limit our maps to regions with mostly dense gas, i.e., the Gulf of Mexico and the Pelican Head. These regions are outlined with white boundaries in Figure 1.

CARMA high-resolution molecular line observations are critical for examining the molecular gas/HII region interactions. However, the analysis of the feedback mechanism also requires an understanding of the effects of a massive star on the overall star formation process. We have therefore complemented our molecular line imaging program with studies of the relationship between the molecular gas and YSOs, using Rebull’s comprehensive YSO catalog (Rebull et al. 2011, hereafter R11).

In this paper, we aim to create a 3-dimensional view of the NAP complex through a comparison of multi-wavelength images. By pinpointing the interaction between the molecular gas and the HII region, especially elevated dust emission associated with molecular gas, we aim to distinguish the line-of-sight locations of the molecular gas clouds relative to the HII region. We also study the number and distribution of YSOs in the associated molecular gas in order to shed light on how star formation is impacted by the feedback.

2. OBSERVATIONS AND DATA COMBINATION

Table 1. Final sensitivity

Transition	Beam	PA	Δv	σ_K
		(deg)	(km s ⁻¹)	(K)
¹² CO(1-0)	7" × 6"	75	0.25	1.1
¹³ CO(1-0)	7" × 6"	75	0.16	0.8
C ¹⁸ O(1-0)	7" × 6"	75	0.16	0.7

As already noted, the NAP region is an example of a relatively simple configuration of a star-forming molecular cloud, young massive star, and associated HII region. The areas of the Gulf of Mexico and Pelican Head mapped by CARMA observations are shown in Figure 1. These were selected to highlight the most dense gas.

2.1. Observations

CARMA observations were carried out in 2017 during the last season of array operations. The instrument set-up was the same as that adopted for the CARMA-NRO Orion Survey (Kong et al. 2018, hereafter K18). Briefly, the 15-element array of six 10-m diameter and nine 6-m antennae was used to map the area of interest. The total mosaicked area of about 1 deg² is made up of 126 pointings of 6' × 6' subfields. The ‘D’ and ‘E’ configurations of the array led to uv-coverage between 2.5-40 kλ, where λ is 2.6 mm for ¹²CO(1-0), resulting in an angular resolution of about 7" (see Table 1).

As for the Orion Survey, the spectral line setup focused on ¹²CO(1-0), ¹³CO(1-0), C¹⁸O(1-0) but also included the CN N=1-0, J=3/2-1/2, SO 2(3)-1(2), and CS(2-1) lines. Here we report only on the ¹²CO(1-0), ¹³CO(1-0), and C¹⁸O(1-0) observations. For ¹²CO the correlator set-up provided a bandwidth of 31 MHz (81 km s⁻¹) and a spectral resolution of 98 kHz (~ 0.25 km s⁻¹). For the other spectral lines, a bandwidth of 8 MHz (~ 21 km s⁻¹) with spectral resolution 24 kHz (~ 0.067 km s⁻¹) was used.

To compensate for the fact that the interferometer observations did not include baselines shorter than 2.5 kλ, effectively filtering out emission from structures larger than 100", the CARMA observations were combined with single-dish maps of the same regions. These were obtained at the Purple Mountain Observatory Delingha 13.7m telescope (hereafter DLH14) (Zhang et al. 2014, hereafter Z14), and are part of the Milky Way Imaging Scroll Painting project (Su et al. 2019).

2.2. Data Combination

The CARMA and DLH14 data were combined in the uv plane, following the procedures outlined in Koda

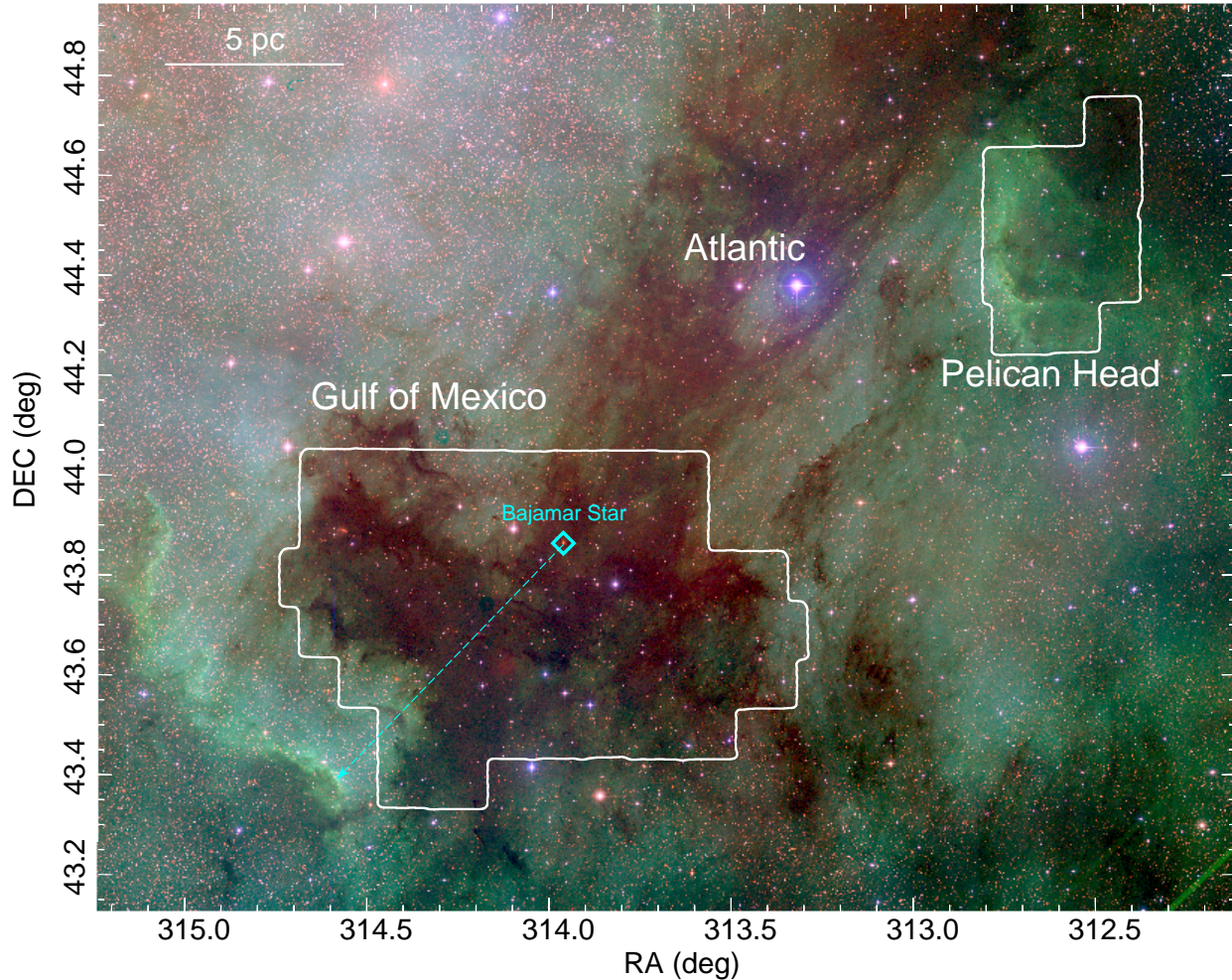


Figure 1. The footprint of the CARMA NAP map (white boundaries) overlaid on a POSS-II false color RGB image using the $0.9\mu\text{m}$ (Red), $0.7\mu\text{m}$ (Green), and $0.43\mu\text{m}$ (Blue) bands. The observed regions include the Gulf of Mexico (the dark area to the southeast) and the Pelican Head (the area to the northwest). The cyan diamond marks the position of the O star confirmed by Comerón & Pasquali (2005). The cyan arrow points from the O star to the two boomerang features at the south-east corner. The scale bar is derived assuming a 800 pc distance to the NAP complex (§4.3).

et al. (2011) and Kong et al. (2018). The resulting images are based on observations that range from zero-spacing fluxes to measurements on the maximum baselines provided by CARMA. Figure 2 shows a comparison of CARMA and DLH14 uv sensitivities. The uv-plane pixel sensitivity as a function of baseline length was calculated following appendix C in Koda et al. (2011). It is a function of the image-plane sensitivity and the dish size or, for an array, baseline length.

In general, to ensure good resulting imaging quality when combining observations from two instruments, it is desirable that the sensitivities match where the baselines overlap. Figure 2 shows this is not the case here; the sensitivity of the DLH14 data is much lower than that of CARMA. The sensitivity mismatch also affects flux scale determination adversely. As described in Kong

et al. (2018), the relative fluxes of the single-dish data and the CARMA can be calibrated based on the flux ratio within the overlapping baselines. Here, the DLH14 data is sufficiently noisy beyond baselines of $2\text{ k}\lambda$, that no meaningful flux scale factor can be established (so we adopt the factor of 1). Nevertheless, as we demonstrate below, the DLH14 observations add a useful contribution to our final images despite their quantitative issues. Table 1 summarizes the final sensitivity for the combined data. To match the single-dish observations, a spectral resolution of 0.16 km s^{-1} was adopted for the combined ^{13}CO and C^{18}O data set.

2.3. Image Quality

To allay concerns about the reliability of the NAP images that result from combining CARMA and DLH14 observations, we compare ^{12}CO integrated intensity im-

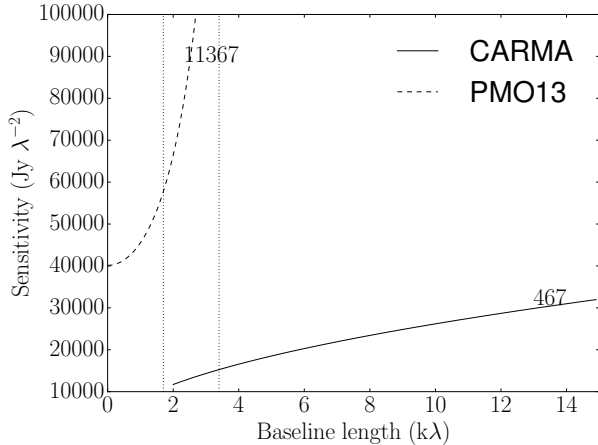


Figure 2. Visibility sensitivity as a function of uv-distance for both DLH14 (dashed curve) and CARMA (solid curve). The imaging sensitivity is labeled next to the curves in units of mJy as in Koda et al. (2011). The vertical dotted lines mark the overlapping region between the two datasets.

ages of the Pelican Head region from DLH14, CARMA, and combined CARMA+DLH14 data. The Pelican Head area was selected since it appears to encompass multi-scale structures (see Figure 3). The DLH14 map (left panel) shows smooth, extended emission with very little structure, while the CARMA map (middle panel) is irregular and prominently shows the (sharp) edges of the cometary-like cloud in this region. The combined image (right panel) clearly displays the usefulness of adding short spacing flux information; considerably more structure appears to be present, both in the edges and body of the cloud.

Following the CARMA-NRO Orion Survey (K18), we carry out a Δ -variance analysis (Stutzki et al. 1998; Ossenkopf et al. 2008) for the channel maps and integrated intensity maps to examine the quality of the data combination. All main features are visible in the integrated intensity maps. Figure 4 shows the Δ -variance spectra for the Pelican Head (left panel) and the Gulf of Mexico (right panel) regions. In both regions and for all tracers, there is a structural break at a scale of $1' - 2'$, corresponding to the gap in our spatial sensitivity at $1.7 - 3.4\text{k}\lambda$ due to the lack of sensitivity at these scales (see Figure 2). The dip in the Δ -variance at that scale also reflects the mismatch of sensitivity in the overlapping baseline lengths.

3. RESULTS

3.1. Feedback Features in IR and the Ionizing Source

Figure 5 shows a composite image of the Gulf of Mexico and Pelican regions (same area shown in Figure 1) made from Spitzer data at $24\mu\text{m}$ (red), $8\mu\text{m}$ (green),

and $4.5\mu\text{m}$ (blue). Figure A1 shows a WISE three-color composite image of the same region in which we assigned red for the $22\mu\text{m}$ emission, green for the $12\mu\text{m}$ emission, and blue for the $4.6\mu\text{m}$ emission. As in Figure 1, We show the extent of the CARMA maps with white boundaries.

In both Spitzer and WISE images, the Gulf region shows a few relatively bright-rim structures. These bright rims trace hot dust in the area. For instance, the WISE W4 band ($22\mu\text{m}$) traces the warm dust thermal radiation. Meanwhile, the WISE W3 band ($12\mu\text{m}$) includes many emission features from PAH (at $7.7\mu\text{m}$, $8.5\mu\text{m}$, $10\mu\text{m}$, and $11.3\mu\text{m}$) and fine-structure lines from [Ne II] ($12.8\mu\text{m}$) and [Ne III] ($15.6\mu\text{m}$). These lines are likely pumped by UV emission (Allamandola et al. 1989) and are believed to be good indicators of star formation and stellar feedback (e.g., Ho & Keto 2007). In any case, the hot dust should be heated by a nearby ionizing source.

Here we argue that the ionizing source responsible for the bright rims seen in these IR images is the Bajamar Star simply because of the proximity of this high-mass, UV-irradiating young star to these features. As will be shown in §3.2, the labeled bright rims that are inside the CARMA map have clear molecular line counterparts. They provide the key connection between the molecular gas and the massive star feedback. Hereafter, we name the bright-rim filamentary structures west and south of the Bajamar Star as Rim1, Rim2, and Rim3. We denote the bright-rim structures with a boomerang-like morphology to the south-east of the Bajamar Star as Boomerang1 and Boomerang2. There are a few more bright-rim structures in the infrared images which we do not label as they are less prominent or do not have molecular line counterparts.

The morphology of the bright-rim structures can also be used to deduce that the Bajamar Star is the most likely source of feedback in this region. A line that passes through the centers of the two boomerang structures and extends to the north-west passes through the position of the Bajamar Star (see the cyan arrow in Figures 1 and 5). There are two more arc-like features to the northeast of Boomerang2. These features, which are not as bright as Boomerang2, point towards the general direction of the Bajamar Star (see Figures 1 and 5).

As stated earlier, there is evidence that the Bajamar Star is the main ionizing source in the Gulf region. Straizys & Laugalys (2008, hereafter SL08) reported 12 additional massive star candidates in the NAP. We determined the distances to these massive stars (including the Bajamar Star) from the Gaia DR2 results (Bailer-Jones et al. 2018). The Bajamar Star (star #8 in SL08)

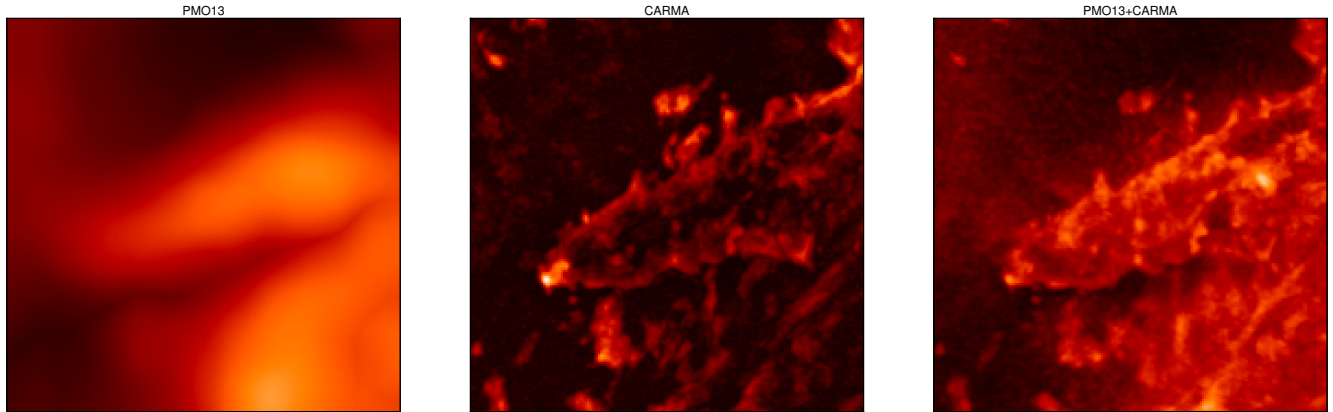


Figure 3. Comparison between DLH14, CARMA and combined images. *Left:* DLH14 peak intensity image. *Middle:* CARMA image. *Right:* Combined CARMA+DLH14 images. All panels show the same 6' by 6' (1.4 pc by 1.4 pc) area centered around Comet1.

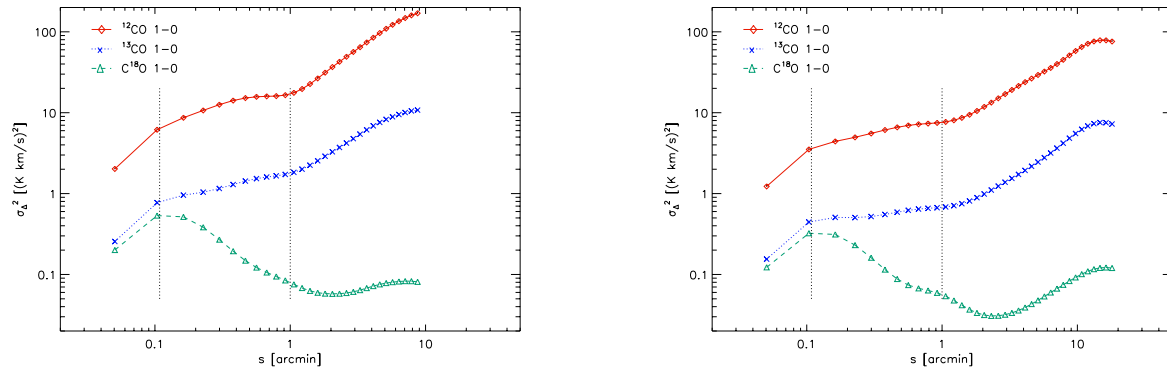


Figure 4. Δ -variance spectra for the $^{12}\text{CO}(1-0)$, $^{13}\text{CO}(1-0)$, and $\text{C}^{18}\text{O}(1-0)$ integrated intensity maps from the combined (CARMA+DLH14) dataset. The x-axis shows the scale measured by the wavelet size. The y-axis displays the variance of the structural fluctuations in the maps at that scale in units of the square of the measured map. The left figure shows the results for the Pelican Head region, the right figure for the Gulf of Mexico. The vertical dotted lines show the scales of the CARMA beam ($\sim 6''$) and the DLH14 beam ($\sim 60''$).

has a distance of 668_{-35}^{+39} pc. However, updated results based on Gaia EDR3 find a distance to the Bajamar's star of $d = 785 \pm 16$ pc, in excellent agreement with the 3D dust and YSO-based results which we discuss in §4.3. The IRS4 source (star #2 in SL08) in the Pelican region (Bally & Scoville 1980) has a distance of 799_{-157}^{+255} pc. However, SL08 suspected that IRS4 is a carbon star. All other candidates are beyond 1500 pc, and there are two sources with no Gaia distances (star #11 in SL08, a.k.a. 2MASS J20580673+4355141; and star #12 in SL08, a.k.a. 2MASS J20582424+4356386). As shown in Figure 1 of B14, these two sources are far to the east of the Bajamar Star. Given the alignment between the Bajamar Star and the bright-rim features discussed above, the Bajamar Star is likely the only massive star responsible for these feedback features in the Gulf region.

We further argue that the Bajamar Star is the main ionizing star impacting the Pelican region as well, as suggested by Damiani et al. (2017). The Pelican Head region is clearly being impacted by UV radiation. In Figures 5 and A1 we notice that the Pelican Head region has very bright infrared emission (mostly notable at $\lambda \gtrsim 5\mu\text{m}$, i.e., visible in IRAC band 3 at $5.7\mu\text{m}$ but barely seen in WISE band 2 at $4.6\mu\text{m}$). The same region also has plenty of H_2 fluorescent emission caused by UV emission (as reported by B14), which matches well with the infrared filaments here. In addition, as discussed in §3.2, there are two bright emission features with a comet-like (i.e., head-tail) morphology in the Pelican Head region which were very likely caused by feedback from a massive ionizing star and point in the general direction of the Bajamar Star. Hereafter, we therefore assume all the feedback features are the result of feedback from the Bajamar Star.

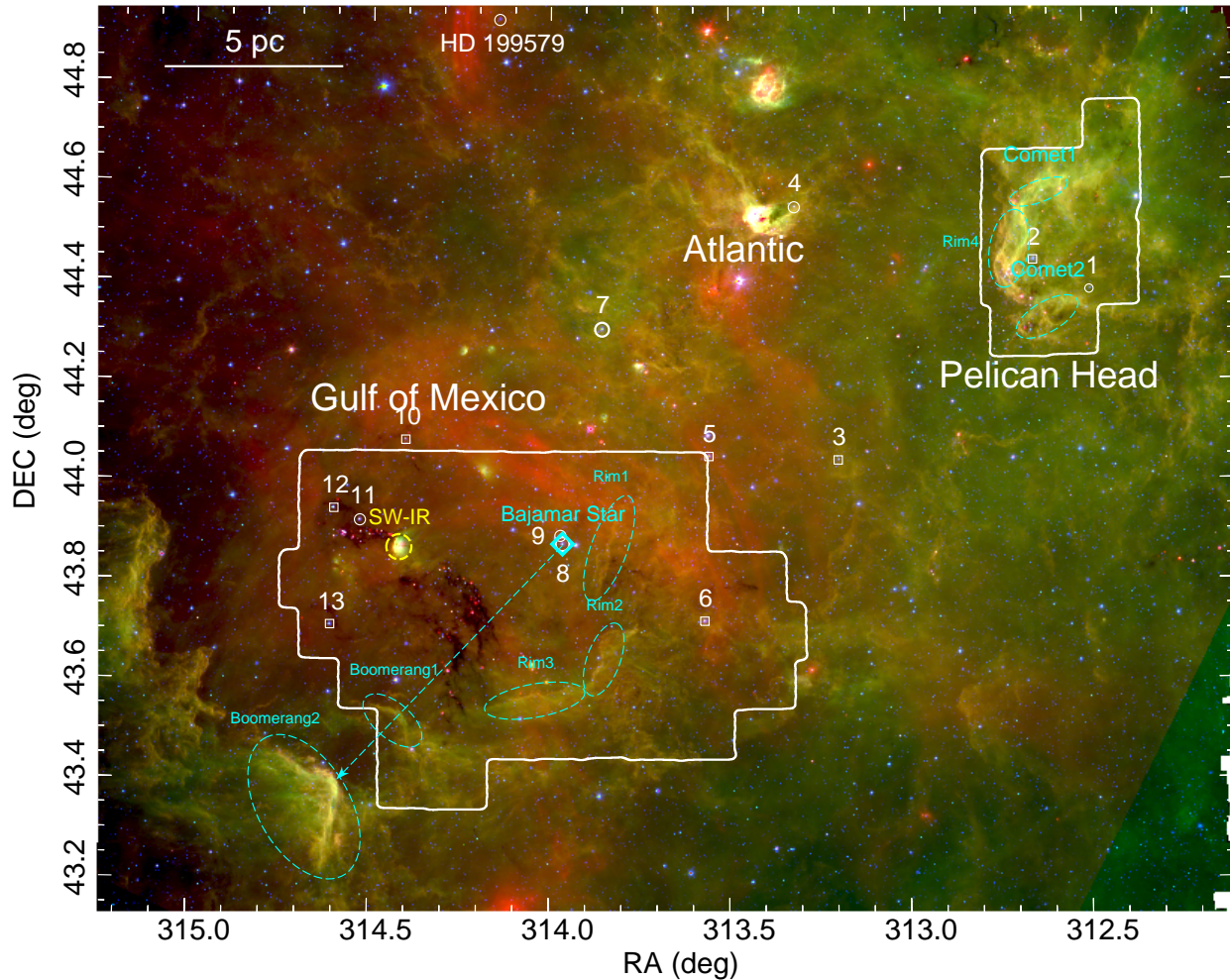


Figure 5. Spitzer false color RGB image using the MIPS $24\mu\text{m}$ band (Red), and the IRAC $8\mu\text{m}$ (Green), and $4.5\mu\text{m}$ (Blue) bands. The images are results from Spitzer program 20015 and program 462 (PI: L. Rebull, see R11). The cyan diamond marks the position of the Bajamar Star. The cyan arrow points south-east from the Bajamar Star to the bright-rim feature with a boomerang-like morphology. The cyan dashed ellipses mark several feedback features discussed in the text (and seen in molecular gas in Figures 6 and 8). The white boundaries show the footprint of the CARMA NAP map. The stars with numbers 1-13 are from SL08 (as shown in B14). Circles are stars classified as spectral type OB. Squares are possible AGB stars (see SL08 and B14). The Bajamar Star is #8.

3.2. Gas Distribution

As can be seen in the ^{12}CO and ^{13}CO moment 0 maps of the Gulf region (Figures 6(d) and 6(e)), there is molecular gas practically over the entire area. There is only notable decrease in emission towards the southeast corner (near the Boomerang1 structure) and towards the northern-central edge of the map. There are also a number of bright prominent regions throughout the maps. These are seen better in the peak intensity maps shown in Figures 6(a) and 6(b) and discussed below. In contrast, the C^{18}O emission is concentrated in the central-eastern part of the map (Figures 6(c) and 6(f)). This emission, as discussed below, coincides with the denser

parts of the cloud where 1.1 mm dust continuum emission has been detected.

Figures 6(a)-6(c) show the peak intensity maps of $^{12}\text{CO}(1-0)$, $^{13}\text{CO}(1-0)$, and $\text{C}^{18}\text{O}(1-0)$ for the Gulf region. We overlay the Bolocam Galactic Plane Survey (BGPS) 1.1 mm continuum emission (Ginsburg et al. 2013), shown in white contours. In the Gulf region, the figures show there is a group of six prominent continuum sources toward the east side of the maps. They are all part of the group of cores traced in 1.1 mm continuum emission labeled as “Gulf total” by B14. This includes the two cores named “Core E” and “Core W” in the northeast part of the map. South of Core W lies the “SW1” core, and towards the southwest of SW1 lie (from north to south) the “SW2 main”, “SW2 SE”,

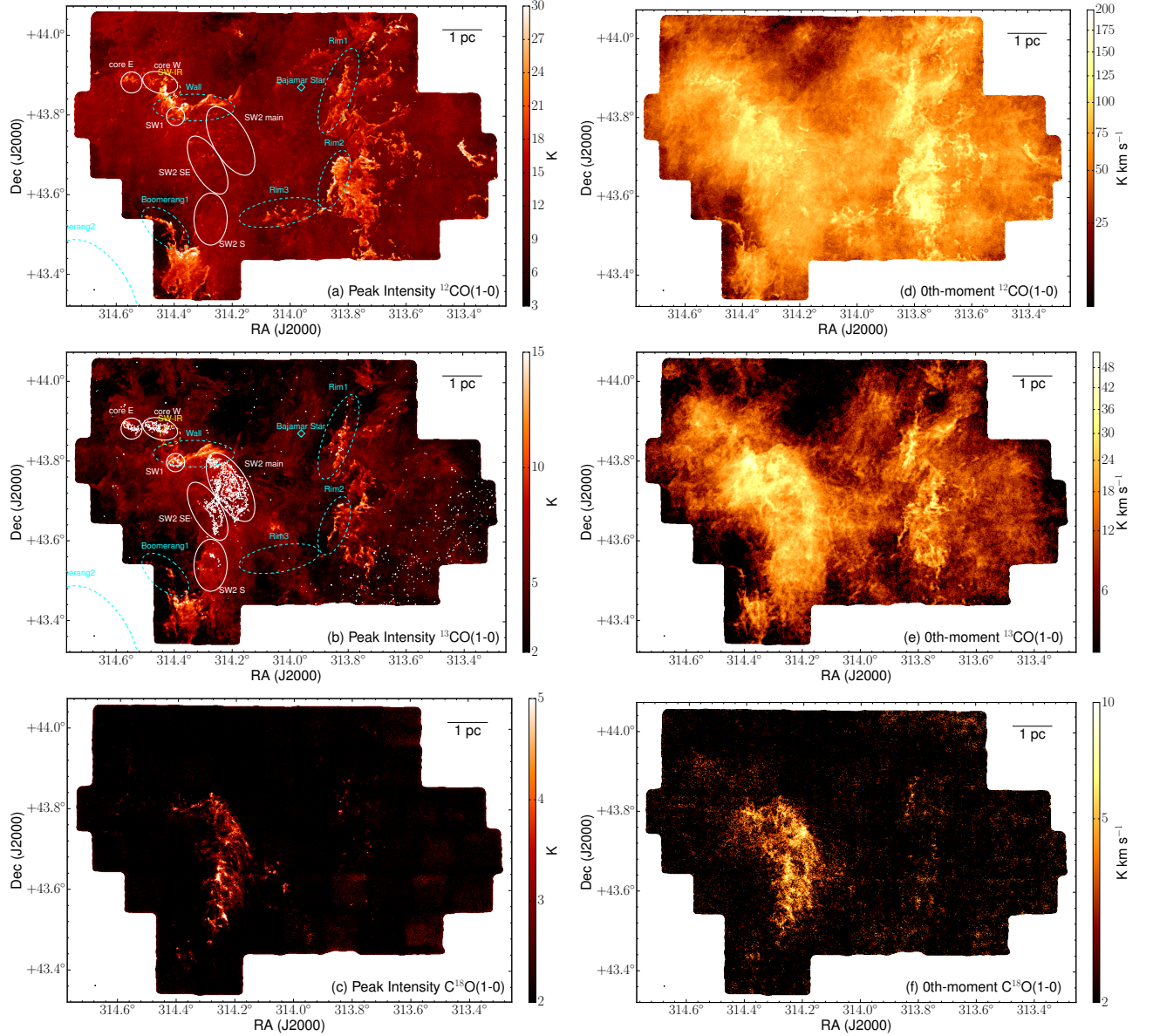


Figure 6. (a): ^{12}CO peak intensity map for the Gulf region. The synthesized beam is at the lower-left corner. The white ellipses are the BGPS cores defined in B14. The cyan ellipses are the same as in Figure 5. (b): ^{13}CO peak intensity map for the Gulf region. The white contours show the BGPS 1.1 mm continuum, starting from 0.4 Jy beam^{-1} and increasing with steps of 0.5 Jy beam^{-1} . (c): C^{18}O peak intensity map for the Gulf region. (d): ^{12}CO 0th-moment map for the Gulf region. The synthesized beam is at the lower-left corner. (e): ^{13}CO 0th-moment map for the Gulf region. (f): C^{18}O 0th-moment map for the Gulf region.

“SW2 S” cores (B14). These last three (the SW2 cores) have prominent C^{18}O counterparts (Figure 6(c)).

There are various prominent features of bright molecular line emission in the Gulf region. Between continuum cores W and SW2 main lies a region of high ^{12}CO and ^{13}CO emission that mostly extends from east to west which we call the “Wall” (see Figure 6(a) and 6(b)). It is likely that the Wall, which is at least twice as bright as the average emission in the rest of the map, traces the warm gas heated by a young star that lies just north of

this structure and is responsible for a bright IR nebula (hereafter SW-IR) seen in Figures 5 and A1.

Additional prominent line emission regions can be seen in the south-east corner and the mid-west part of the map. In the south-east, the bright emission is coincident with the Boomerang1 feature discussed above (see §3.1 and Figure 5). In the central-western region of the map, the bright emission is associated with the IR features labeled Rim1, Rim2 and Rim3 (see Figure 5 and §3.1). These, in general, show a sharp increase in

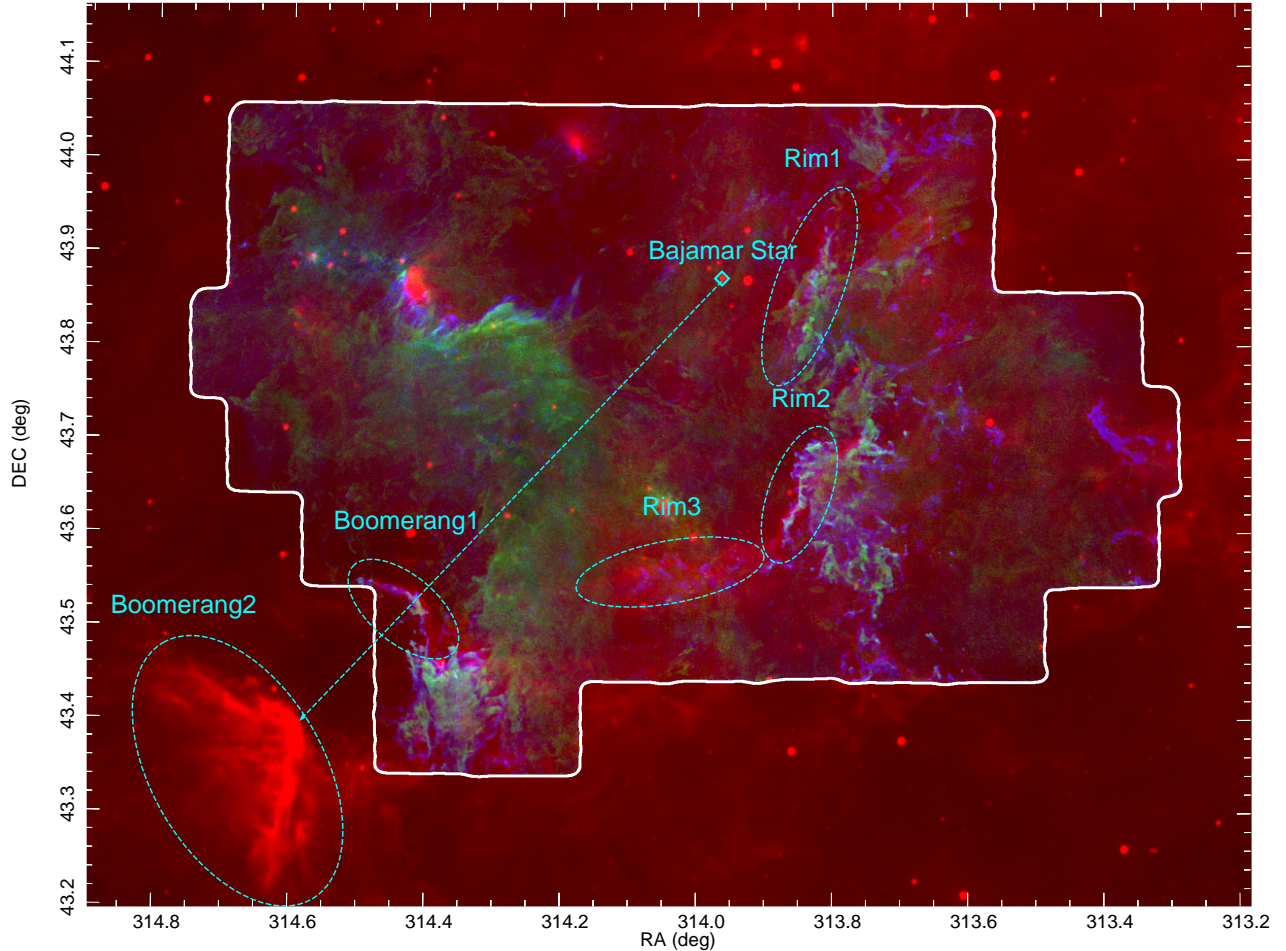


Figure 7. RGB false-color image including the WISE 12 μm band (red), the peak intensity map of $^{13}\text{CO}(1-0)$ (green), and the peak intensity map of $^{12}\text{CO}(1-0)$ (blue). The cyan ellipses mark the locations of the feedback features in Figure 5. They match well with the thin CO filaments in the region covered by our CARMA observations.

intensity towards the edge of the emission structure facing the Bajamar Star (aligning with the IR bright rims defined in §3.1 and Figure 5) and have a chaotic morphology in ^{12}CO (Figure 6(a)) and ^{13}CO (Figure 6(b)) away from these bright rims. As discussed later, these structures are part of the filament F-1 defined in the study by Z14.

We show a three-color image in Figure 7 comparing the WISE 12 μm band, the peak intensity map of ^{13}CO , and the peak intensity map of ^{12}CO . It is very clear that the bright-rim features in the IR image are associated with the bright filaments in molecular line emission. Rim3 overlaps with ripple-like features in CO emission. Moreover, the entire molecular gas structure that connects with the rims appear as shredded pieces. A plausible explanation is that the expanding bubble has reached (or is very close to) the molecular gas associated with these structures, and the gas has this chaotic morphol-

ogy because it is being dispersed by the UV photons from the massive star.

In the Pelican Head region, we detect ^{12}CO (Figure 8(a)(d)) throughout most of the mapped area which roughly follows a morphology similar to the structure delineated by the yellow-colored features in the Spitzer and WISE three-color composite images. The ^{12}CO , ^{13}CO and C^{18}O integrated intensity maps (Figures 8(d) to 8(f)) show three separate regions of relatively high-intensity emission: in the north (around decl. 44.58°), center (around decl. 44.43°), and south (around decl. 44.3°). These structures are also clearly seen in the peak intensity maps (Figures 8(a) to 8(c)). The northern and southern high-intensity regions (which we name Comet1 and Comet2, respectively) have comet-like structures with bright narrow heads and with tails extending to the northwest. The central high-intensity structure (which we name Rim4) has a wide arc-like edge and extended (bright) emission to the west, somewhat

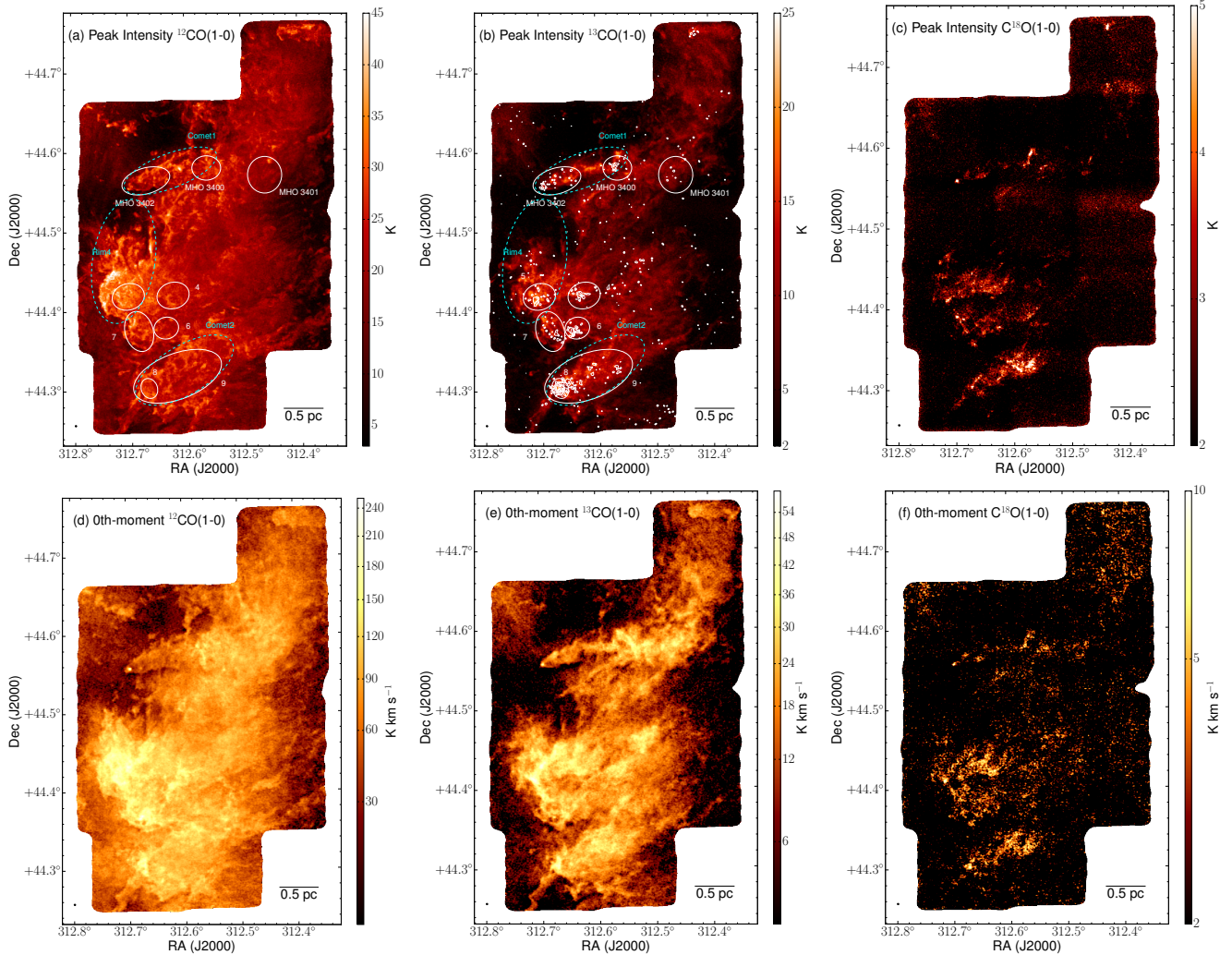


Figure 8. (a): ^{12}CO peak intensity map for the Pelican region. The synthesized beam is at the lower-left corner. The white ellipses are the BGPS cores defined in B14. The cyan ellipses are the same as in Figure 5. (b): ^{13}CO peak intensity map for the Pelican region. The white contours show the BGPS 1.1 mm continuum, starting from 0.4 Jy beam^{-1} and increasing with steps of 0.5 Jy beam^{-1} . (c): C^{18}O peak intensity map for the Pelican region. (d): ^{12}CO 0th-moment map for the Pelican region. The synthesized beam is at the lower-left corner. (e): ^{13}CO 0th-moment map for the Pelican region. (f): C^{18}O 0th-moment map for the Pelican region.

similar to the Rim2 structure in the Gulf region. All these features roughly point toward the Bajamar Star, and thus very likely caused by feedback from the massive star.

Comet1 is shown in detail in Figure 3. The CARMA high-resolution data shows some ripples at the boundaries of Comet1 (especially the northern boundary). Interestingly, both cometary clouds have BGPS sources at their head location, reminiscent of triggered star formation by radiatively driven implosion (Bertoldi 1989). The northern one corresponds to the “Pelican MHO 3402” core in B14 (Figure 3, Table 4), while the southern one corresponds to the “Pelican 8” core in B14.

3.3. Gas kinematics

Figures 9(a) to 9(c) show the intensity-weighted average velocity (1st-moment) maps of the Gulf region. They show a general picture of the complex kinematics in this region. In the ^{12}CO and ^{13}CO 1st-moment maps (Figures 9(a) and 9(b)), the molecular gas associated with the IR-bright rims (i.e., Rim1, Rim2) can be seen as gas with average velocities of about -5 km s^{-1} , in sharp contrast with adjacent gas at more redshifted velocities.

In contrast to the Gulf region, the Pelican Head region (Figures 10(a) to 10(c)) shows a significantly narrower range of intensity-weighted average velocities. Here most of the emission is concentrated at velocities between -2 and 2 km s^{-1} . In the ^{13}CO 1st-moment map (Figures 10(b)), Comet1 is discernible as an oval region

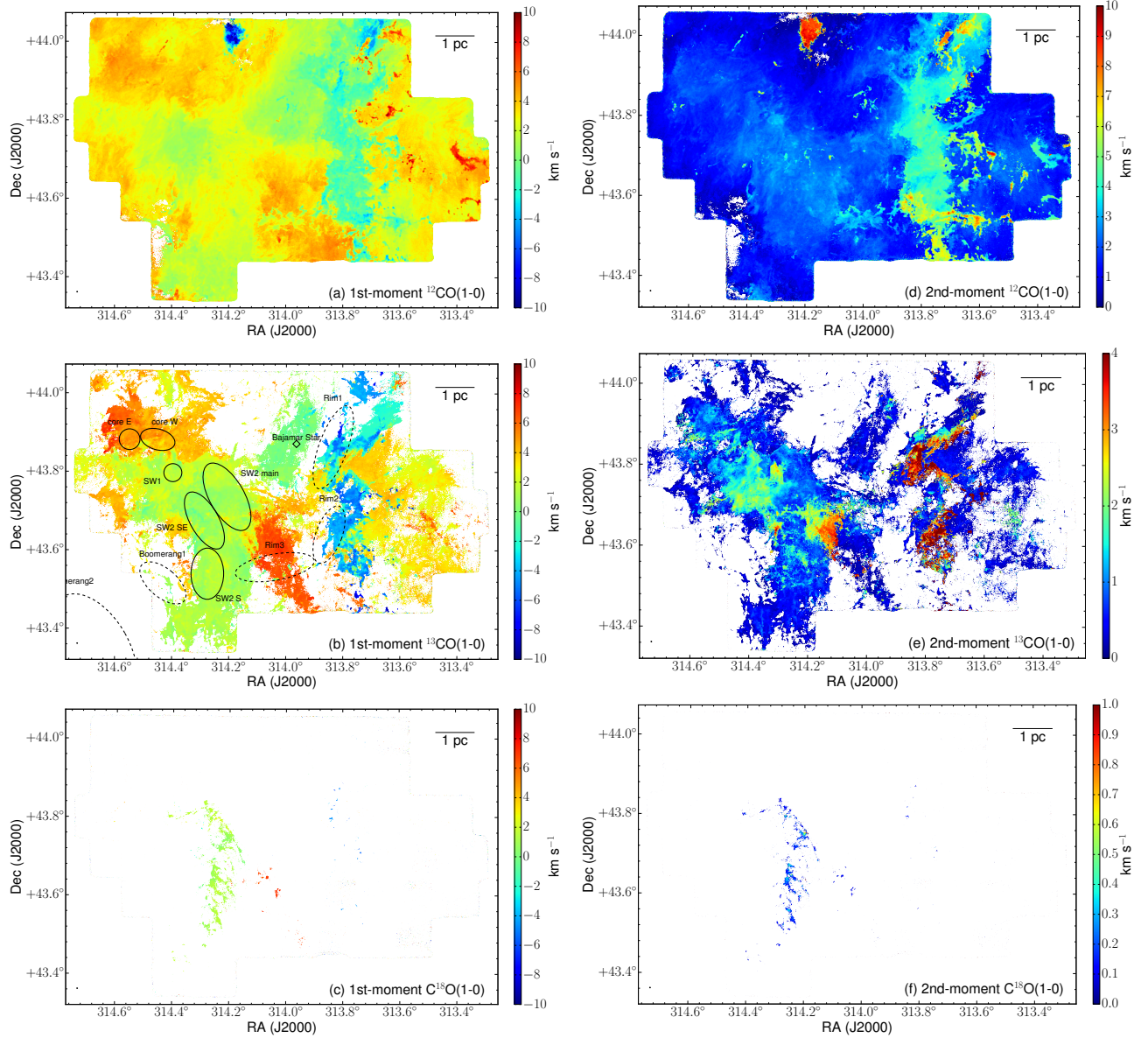


Figure 9. (a): ^{12}CO 1st-moment map for the Gulf region. The synthesized beam is at the lower-left corner. (b): ^{13}CO 1st-moment map for the Gulf region. The ellipses with black solid lines are the BGPS cores defined in B14. The dashed ellipses are the same as the cyan ones in Figure 5. (c): C^{18}O 1st-moment map for the Gulf region. (d): ^{12}CO 2nd-moment map for the Gulf region. The synthesized beam is at the lower-left corner. (e): ^{13}CO 2nd-moment map for the Gulf region. (f): C^{18}O 2nd-moment map for the Gulf region.

with velocities around 2 km s^{-1} . Comet2 and Rim4 structures are not as conspicuous as Comet1, but are similar to the other feedback features in the NAP, in that the gas beyond the sharp edge is at redshifted velocities compared to the feedback structure.

Figures 9(d) to 9(f) show the 2nd-moment maps of the Gulf region. In the ^{12}CO and ^{13}CO maps (Figures 9(d) and 9(e)), the gas associated with the bright rims shows large velocity dispersion. On the other hand, the C^{18}O gas (Figure 9(f)) has narrow velocity widths, in sharp contrast with the ^{12}CO and ^{13}CO gas. Figures 10(d) to

10(f) show the 2nd-moment maps of the Pelican region. The gas facing the Bajamar Star shows larger velocity dispersion. The gas behind this front is more quiescent. Interestingly, Comet1 does not show large dispersion in either ^{12}CO or ^{13}CO maps.

3.4. Gas Structures Around W80

The moment maps by themselves are not enough to differentiate among the different cloud components. The distribution of dark patches in the optical image of the region in concert with the location and kinematics of

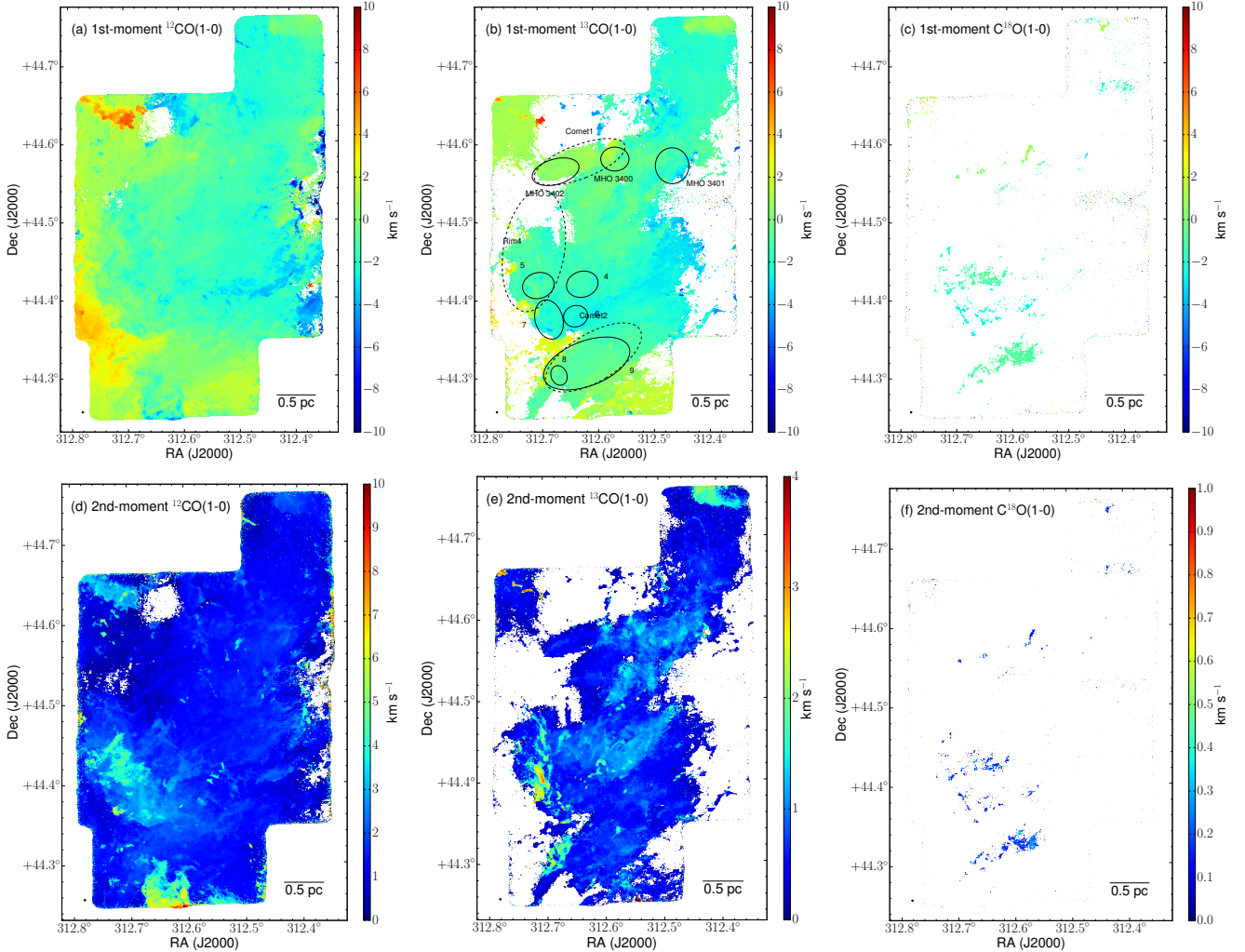


Figure 10. (a): ^{12}CO 1st-moment map for the Pelican region. The synthesized beam is at the lower-left corner. (b): ^{13}CO 1st-moment map for the Pelican region. The ellipses with black solid lines are the BGPS cores defined in B14. The dashed ellipses are the same as the cyan ones in Figure 5. (c): C^{18}O 1st-moment map for the Pelican region. (d): ^{12}CO 2nd-moment map for the Pelican region. The synthesized beam is at the lower-left corner. (e): ^{13}CO 2nd-moment map for the Pelican region. (f): C^{18}O 2nd-moment map for the Pelican region.

the molecular gas can be used to derive an approximate three-dimensional distribution of the gaseous structures observed in our map.

The dark patches in the optical image of the NAP in Figure 1, particularly the Gulf and Atlantic regions, have been generally thought to be caused by molecular clouds in front of the HII region, mostly at the same distance (B14, Z14). However, a closer look at Figure 1 suggests a more complicated story. The dark clouds in this image show at least two shades of darkness. One is a semi-transparent gray silhouette that runs from the top-right (northwest) edge of the figure throughout the Atlantic area, extending south of the Bajamar Star.

A large area southeast of the Bajamar Star also shows this semi-transparent grayish hue. We call areas with this shade as “gray regions”. In Figure 1, we also see a

collection of patchy clumps that are much more opaque than the gray regions, which traverse from east to west across the entire Gulf region. We name these “dark regions”. The two different shades, combined with the information from images at other wavelengths (and the gas kinematics), imply that there may be more than one group of molecular gas (possibly at different distances) along the line of sight, consistent with our implications based on the kinematics information. Determining the relation between these two groups of clouds is important for identifying the molecular gas responsible for the star formation that is taking place in this region and for understanding the impact of feedback on the molecular clouds in the NAP.

In §B and Figures B2 to B8, we identify distinctive, coherent features in the ^{13}CO position-position-velocity

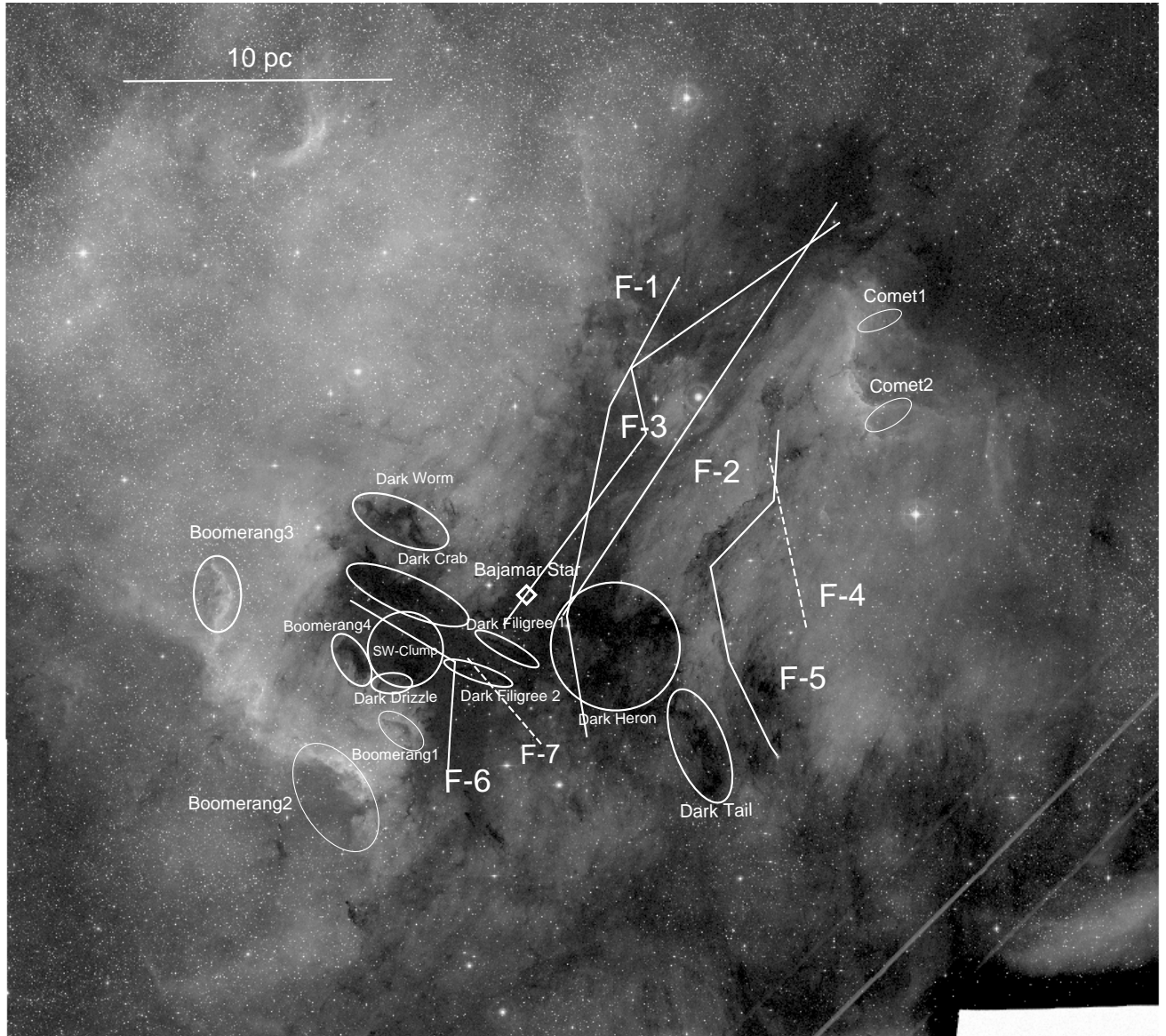


Figure 11. Definition of molecular gas filaments and clumps by comparing the POSS-II red color ($0.7 \mu\text{m}$) and the $^{13}\text{CO}(1-0)$ cubes (§3.4, §B, Table 2). **Background:** POSS-II red color plate. The regions mark the filaments and clumps defined in §3.4 and §B. The filaments with solid lines are in the foreground. Those with dashed lines are behind the bubble. Filaments F-1, F-2, F-3, F-4 were defined in Z14. The green boundaries show the CARMA mosaic footprints.

(PPV) cube, and compare the gas distribution with different features seen in the POSS-II red color plate. Figure 11 summarizes the major structures defined based on this comparison.

4. THREE-DIMENSIONAL STRUCTURE

The most useful information from the small-scale structures (captured by CARMA) is the morphology matching with the bright infrared rims. The matching between F-1 and the rims confirms that the rims are part of the molecular filament. This finding shows that

the filament is being heated and dispersed by the massive star. The morphology match between the molecular filament and the gray regions in the POSS-II image thus reveal that the gray regions in the optical images likely trace foreground molecular gas that is being destroyed by the Bajamar Star, and therefore very close to the expanding bubble. As a result of this, the three-dimensional picture of the entire NAP becomes clearer.

4.1. Three-dimensional structure of the NAP complex

North America and Pelican Nebula Molecular Gas Relative Locations

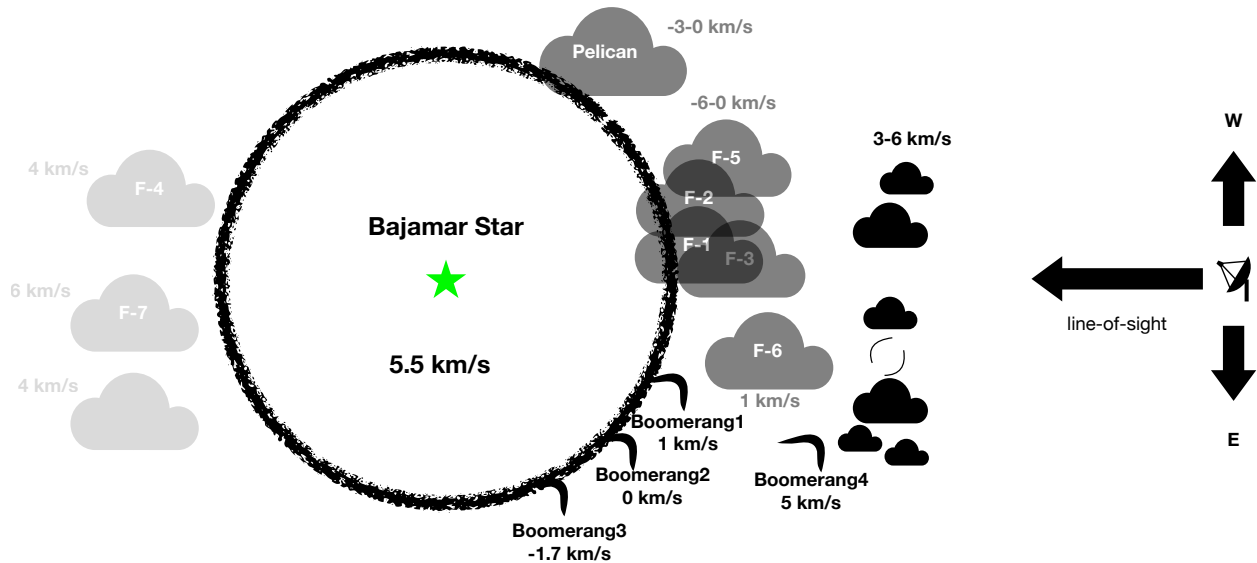


Figure 12. The line-of-sight locations of the filaments and clumps relative to the W80 bubble (black circle). The Bajamar Star is at the center of the bubble. Three groups of clouds are shown, including the far side clouds (F-4, F-7, and another clump to the northeast of the Gulf region, see §3.4 and Figure B6), the foreground contacting gray-clouds, and the foreground dark clumps and filigrees (closest to the observer). The LSR velocities of the clouds are also included. We assign a velocity of 5.5 km s^{-1} for W80 based on the radio recombination line observation by Lockman (1989).

Figure 12 shows a schematic of the line-of-sight structure of the NAP complex. The locations are in relative sense and are based on the findings from §3.4 and §B. We include major structures that are defined in §B. The structures are mainly in the Gulf and Atlantic regions, with a few in the Pelican region and behind the W80 bubble.

There are three major groups of clumps and filaments based on their line-of-sight distance. The closest to us is a group of dark clumps with varying morphologies (see Figure 11 and the rightmost dark structures in Figure 12). They are in front of the W80 bubble and appear as dark shadows in the POSS-II images. The group members are small and clumpy, with many ~ 10000 AU globules. Their V_{lsr} is similar to that of the bubble.

Between the dark group and the W80 bubble is the group of gray clouds. F-1 is very close to the bubble being part of this group; it is lit in the mid-to-far infrared and shows bright rims (§3.4 and Figures 5, A1, 6, B2). F-2, F-3, F-5 are also close to the bubble, especially in the Atlantic region, based on their similar extinction and velocity as the F-1 filament. F-6 may not be so close to the bubble as F-1, but it is between the bubble and the Dark Crab. Boomerang1 and Boomerang4 appear to be dark in the optical image. They are on the near side of the bubble. Boomerang2 and Boomerang3 are probably on the edge of the expanding bubble.

Behind the bubble, there are several background clumps, including F-4 and F-7. They do not show gray/dark counterparts in the optical images. They are moving away at $\sim 5 \text{ km s}^{-1}$. It is not clear whether they are close to the bubble. We suspect that F-7 (covered by our CARMA observations) is not very close to the HII region as it does not exhibit the “shredded” and chaotic structure seen in F-1.

4.2. Correlation between Gas and Extinction

As an independent approach to associate the different velocity components to structures seen in the optical image as foreground layers we correlate the ^{13}CO data with the foreground extinction. We focus on the combined data in the Gulf region. Instead of using existing extinction maps that trace the whole column of material (e.g. Cambrésy et al. 2002), we obtain an approximate foreground extinction map from the POSS-II red image in Figure 11 by assuming that the highest intensity in the region represents the typical radiation from the bubble and translating all lower intensities into an effective red extinction. The resulting foreground extinction map is shown in the top left panel of Figure 13.

We investigate the correlation between ^{13}CO gas and the extinction by computing the covariance between the

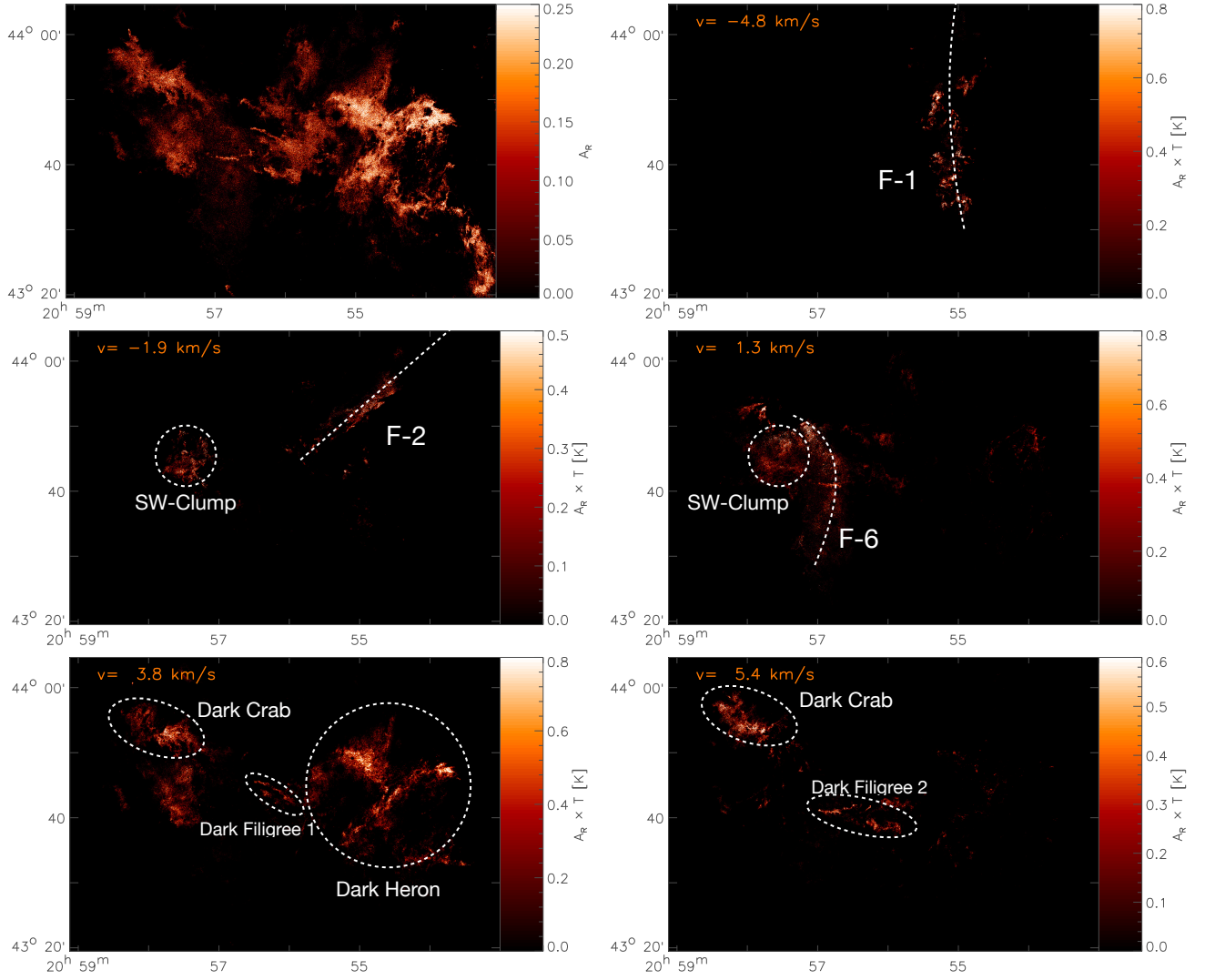


Figure 13. Maps showing the correlation between optical extinction and ^{13}CO emission. **Top Left:** Map of foreground extinction based on the POSS-II red image in Figure 11.1. **Other Panels:** Covariance maps of the foreground with selected ^{13}CO velocity channels. The velocity is labeled at top left corners.

optical image and ^{13}CO channel maps¹. For the ^{13}CO channel covariance maps (shown in 13), only contributions above 4σ of the noise were considered.

We find strong correlation around -5 km s^{-1} (the channel including F-1, Figure B2), -2 km s^{-1} (including F-2, Figure B3), and 4 km s^{-1} (including SW-Clump, Dark Filigree 1, Dark Heron, Figure B6). At 1.3 km s^{-1} (including F-6, Figure B5) and 6.4 km s^{-1} (including Dark Crab, F-7, Figure B8), we actually find a significantly weaker correlation because of additional emission at those velocities stemming from the background. Most importantly, the calculation suggests that

the Dark Crab is a distinct structure from the F-6 filament. Although it appears at the same velocity as the F-7 gas both the dark appearance at near-infrared wavelengths and the well resolved structure indicate that it must represent material in front of the bubble, closer towards us. This is important for being able to match the known YSO clusters in the NAP region with their host molecular gas (see §5.1). Of particular interest is the SW-Clump, which seems to have counterparts at -2 and 4 km s^{-1} . In the molecular line cubes of ^{12}CO and ^{13}CO , we find in fact that this clump spans a wide velocity range, encompassing the velocity of the F-6 filament. The average spectrum of SW-Clump shows two peaks about -2 and 4 km s^{-1} . A possible explanation is that the clump is elongated along the line of sight, and its far side is being pushed by the bubble to produce the

¹ In contrast to the mathematically correct covariance, we do not subtract the mean values before the multiplication of both maps to focus on emission only.

Table 2. Cloud Naming

Name	RA (deg)	DEC (deg)	v_{lsr} (km s ⁻¹)	Figure
F-1	313.64623	44.09655	-4.9	B2
F-2	313.31135	44.36088	-2.7	B3
F-3	313.47317	44.35101	0	B4
F-4	312.99136	43.98752	3.5	B6
F-5	313.11716	43.81911	0	B4
F-6	313.32268	43.60290	0	B4
F-7	314.04069	43.57983	6.5	B8
Boomerang1	314.43230	43.51767	1.5	B5
Boomerang2	314.67420	43.34278	0	B4
Boomerang3	315.10378	43.88507	-2.7	B3
Boomerang4	314.61085	43.70758	4.9	B7
Comet1	312.62712	44.57655	2	3,10
Comet2	312.60718	44.32575	0	10
Dark Crab	314.40155	43.87826	4.9	B7
Dark Drizzle	314.46471	43.64457	4.9	B7
Dark Filigree 1	314.03919	43.73130	3.5	B6
Dark Filigree 2	314.14630	43.66815	4.9	B7
Dark Heron	313.64063	43.73207	3.5	B6
Dark Tail	313.33844	43.46264	3.5	B6
Dark Worm	314.42482	44.07318	3.5	B6
SW-Clump	314.41301	43.73359	3.5	B6

NOTE—F-1, F-2, F-3, F-4 were defined in Z14. Figure 11 shows a summary of the features overlaid on the POSS-II red color image.

negative velocity component. The SW-Clump is likely connected or associated with the F-6 filament.

4.3. Distance to the NAP Region

In this section, we discuss the distance to the NAP based on YSOs, 3D dust mapping, and the presumed ionizing star (Bajamar’s star).

First, we start by using the Gaia distances (Bailer-Jones et al. 2018) of YSOs associated to dark clouds in this region to evaluate the distance to the NAP region. Figure 14 shows an overview of the YSOs in the NAP region from R11. The YSO classification was based on the near- to mid-IR spectral slope (from 2 to 24 μm , see §5.2 of R11)². We cross-matched each of the more than 2000 sources in the catalog of NAP YSOs produced by R11 with the Gaia distance catalog (Bailer-Jones et al.

2018) using a search radius of 2”, and found that a little more than 1000 sources have Gaia measurements.

In Figure 15, we show a histogram of Gaia distances for all R11 YSOs that are available in the Gaia catalog. We zoom in to the range of distances between 0 and 1500 pc, as sources beyond 1500 pc are highly unlikely to be associated with the NAP complex. As shown in the histogram, there is clearly a peak around 800 pc (there is a tail extending from 1500 pc to about 7000 pc, but no other peaks). Assuming the YSOs are close to or associated with the molecular gas in the NAP complex, then the histogram implies these clouds are likely at a distance of ~ 800 pc. Recently, Zucker et al. (2020) reported a similar distance toward the NAP region based on 3D dust mapping. Kuhn et al. (2020) also reached a similar conclusion based on a more detailed study of stellar components of the NAP region.

The estimated distance of 800 pc using the YSOs is at odds with the original distance of 668^{+39}_{-35} pc that we derived to Bajamar’s star based on Gaia DR2 parallax measurements. Even if one considers the upper bound of the uncertainty, the deduced distance would be about 100 pc closer than the distance derived from YSOs or 3D dust mapping. Fortunately, the higher precision astrometry and improved treatment of systematic effects available in Gaia EDR3 has resolved the discrepancy in the previous DR2 parallax measurement, and Kuhn & Hillenbrand (2020) report a new distance to the Bajamar’s star of 785 ± 16 pc.

In panels (b) to (d) of Figure 15, we separately plot the distance histogram for the three clusters defined in R11. Their names are Gulf, Pelican, and PelHat, and we mark their locations with white dashed ellipses in Figure 14. One can see from Figure 15 that all of the three YSO clusters peak at ~ 800 pc. The PelHat cluster has a limited number of members so its distance is uncertain. However, the Gulf cluster, which is associated with the foreground gray/dark features (Dark Crab and F-6, see §5.1), also has a peak distance of ~ 800 pc. Since the W80 region is behind the gray/dark features, the distance to the W80 region must be farther than the Gulf cluster. While this contradicts the Gaia DR2 distance measurement for the Bajamar Star, it is entirely consistent with the more accurate Gaia EDR3 measurement (see Kuhn & Hillenbrand 2020).

We have produced an interactive distance map of the NAP based on 3D dust mapping (available here), following the technique outlined in Zucker et al. (2019, 2020). Figure 16 shows the distribution of dust along the line of sight toward three representative sub-regions (≈ 1 deg² in area) of the map, centered at ($l = 84.0^\circ$, $b = -1.8^\circ$), ($l = 84.4^\circ$, $b = 0.3^\circ$), and ($l = 85.1^\circ$, $b = -0.3^\circ$), re-

² See Fang et al. (2020) for the latest spectroscopic study of the young stars in NAP.

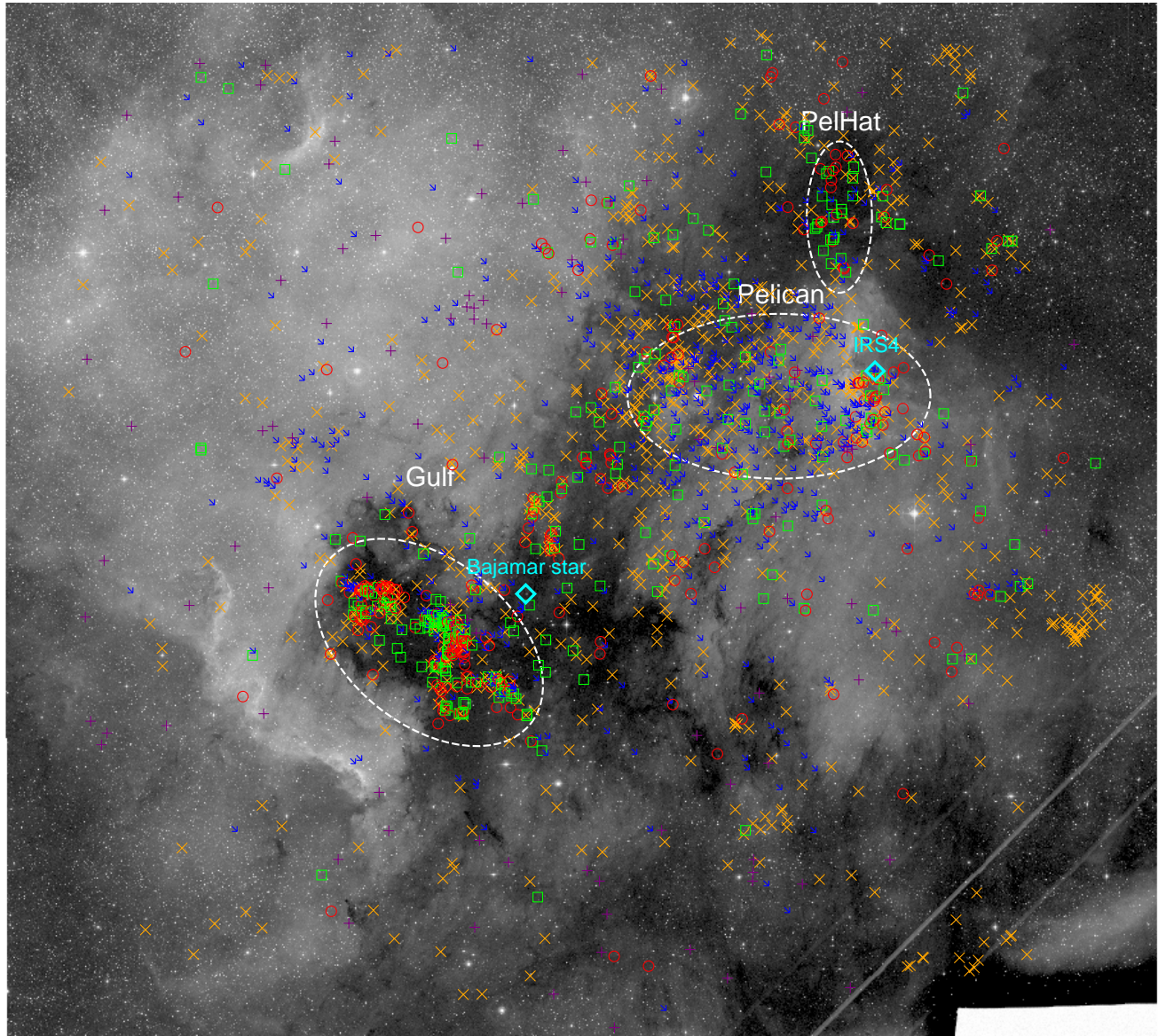


Figure 14. Distribution of young stellar objects in the NAP region. Grayscale background: POSS-II red band image from Figure 1. YSOs from R11 are shown as different symbols: red circle - Class I, green box - Class flat, blue arrow - Class II, purple cross - Class III, orange “x” - unknown. The three white dashed circles mark the locations of the clusters (Gulf, Pelican, PelHat) defined by R11.

spectively. Similar region-by-region plots over the full cloud are available online. The distance uncertainties for the nebula do not include any systematic uncertainties, which we estimate to be 5% in distance.

For the full map, see https://faun.rc.fas.harvard.edu/czucker/Paper_Figures/NorthAmerica.html. To produce the map, we grid the NAP region into individual pixels (based on the Healpix system with a resolution parameter (N_{side}) of 64, Gorski et al. 2005) following Zucker et al. (2019), where each pixel covers about

1 deg^2 on the Sky. Each pixel is color-coded according to the distance we infer for the dust in that sub-region. We are able to target all area with an extinction of at least 5 mag. Each sub-region is fit independently, with a typical uncertainty of about 5–6% in distance or about 40 pc. The distances obtained via 3D dust mapping are complementary to YSO-based distances, obtained either from Gaia DR2 or from VLBI observations (e.g., towards masers; Reid et al. 2019). Zucker et al. (2020) find that their 3D dust mapping approach agrees with

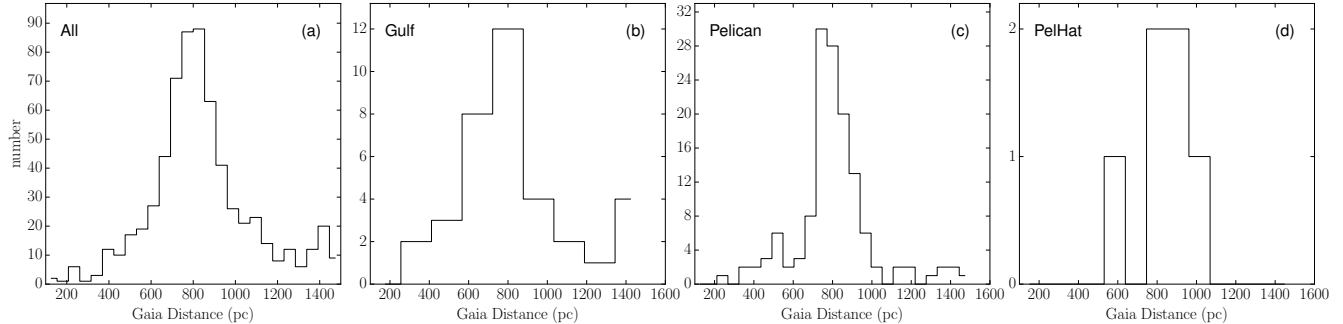


Figure 15. Distribution of (available) Gaia distances to the YSOs identified by R11. Panel (a) shows the histogram for all YSOs in the region. Panels (b) to (d) show the distribution of Gaia distance for the three different clusters in the region. The cluster is identified on the top left corner of each panel. The y-axis shows the number of YSOs in each distance bin. Note that we limit the x-axis to distances between 0 to 1500 pc. YSOs beyond 1500 pc are likely not associated with the NAP complex.

maser distances to within 10% out to 2.5 kpc with no systematic offset.

While it is difficult to definitively constrain distance gradients within the NAP given our typical systematic uncertainty (≈ 40 pc), we determine that the entire NAP region traced by dust is consistent with being at the same distance to within a few tens of parsecs. Using distance information across the full cloud, we find an average distance of 797 ± 40 pc, in excellent agreement with Gaia DR2 distances towards YSOs in Figure 15. Our results are also consistent with the updated distance to Bajamar’s star – the presumed ionizing star – based on recent Gaia EDR3 results (from Kuhn & Hillenbrand 2020), who find $d = 785 \pm 16$ pc.

On a side note, the Gulf cluster distance histogram in Figure 15 shows a tentative excess at $\lesssim 800$ pc, while the Pelican cluster shows a clearer excess at $\gtrsim 800$ pc. This distance difference implies that the Gulf cluster has members that are closer to us, which is consistent with the Gulf cluster being associated with a near-side clump/filament. Indeed, Kuhn et al. (2020) reported that stars in the Gulf region (their group E) are ~ 35 pc closer than stars in the Atlantic and Pelican regions (their groups A to D at ~ 795 pc).

5. DISCUSSION

5.1. Star Formation and Feedback

Out of the three clusters discussed in §4.3, and show in Figure 14, the Pelican cluster does not have a morphological match with molecular gas structures. The Pelican Head region (northwest of the Pelican cluster from R11 and south of the PelHat cluster from R11) has multiple MHOs identified in B14, so the young stars there are still accreting from the molecular gas. However, the rest of the Pelican cluster (outside the Pelican Head region) has very limited $^{13}\text{CO}(1-0)$ or $\text{C}^{18}\text{O}(1-0)$ emission, except for those young stars near the Atlantic region. R11 also noted that the cluster is in a low-extinction re-

gion (based on the extinction map from Cambrésy et al. 2002).

Kuhn et al. (2020) noticed that the Pelican cluster (their Group D) shows evidence of expansion. As discussed in §3.4, the Atlantic clouds are clearly associated with the bright rims, and are likely being dispersed by the Bajamar Star. A possible scenario is that the molecular gas associated with the Pelican cluster, probably the gas in the Atlantic region, is being dispersed by the massive star. The forming cluster was originally confined by the cloud gravitational potential, but now it is expanding due to the (sudden) dispersal of the cloud. If true, then the Pelican cluster is a good example of cluster formation halted by the feedback from a nearby massive star. In other words, the cluster formation reaches an end, not because its associated gas is consumed or dispersed by the cluster itself but by a neighboring massive star.

Here we carry out a simple analysis to test the possibility that the cloud (hereafter the pre-Pelican cloud) in which the Pelican cluster formed can be dispersed by the Bajamar Star. We note that the PelHat cluster (north of the Pelican cluster) overlaps with relatively high extinction regions (see Figure 14). It is at the edge of the W80 bubble, and has ample molecular gas to continue forming stars and feed the accretion of the existing protostars. Indeed, a recent survey of outflows (Zhang et al. 2020) has revealed a few molecular outflows in PelHat, indicating active protostellar accretion. Meanwhile, we know the Pelican cluster has little molecular gas. So the pre-Pelican cloud was probably stripped from the Pelican cluster. Either the pre-Pelican cloud was pushed away by radiation pressure or bubble expansion, or the cloud was ionized by the Bajamar Star. In any case, the Pelican cluster should be closer to the Bajamar Star than PelHat. In other words, the cluster should be inside the bubble by now.

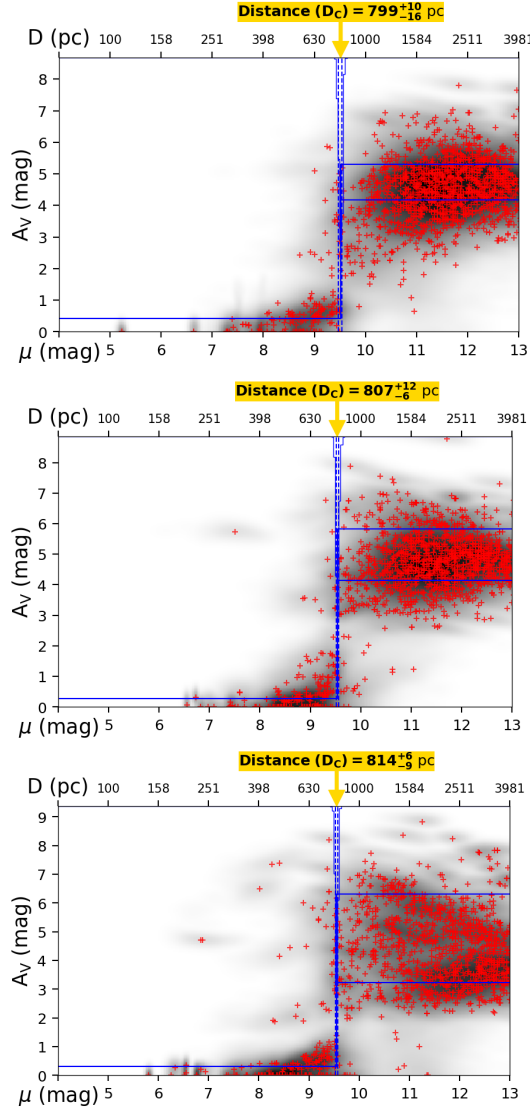


Figure 16. The distribution of dust extinction A_V as a function of distance modulus μ (or distance D) for three sub-regions of the NAP ($\approx 1 \text{ deg}^2$ in area) centered on $(l = 84.0^\circ, b = -1.8^\circ)$ (top), $(l = 84.4^\circ, b = 0.3^\circ)$ (middle), and $(l = 85.1^\circ, b = -0.3^\circ)$ (bottom). The blue line shows the inferred distribution of dust along the line of sight for each sub-region. In each panel, a sharp increase in extinction (marked with a yellow arrow) indicates the most likely distance to that sub-region of the NAP. The red crosses indicate the most likely distance and integrated dust extinction for stars toward each sub-region, which are collectively used to constrain the dust distribution. Based on similar analyses across the full NAP region, we infer an average distance to the cloud of 797 ± 40 pc.

To carry out our basic feedback analysis, we need to estimate and make various assumptions about the HII region and the pre-Pelican cloud. The ionizing photon flux from the Bajamar Star is $S_{UV} \sim 10^{49} \text{ s}^{-1}$ and the electron density n_e of the HII region is $\sim 10 \text{ cm}^{-3}$ (Wendker 1968; Comerón & Pasquali 2005). The ionizing flux S from the Bajamar Star corresponds to a luminosity of $2.2 \times 10^{39} \text{ erg s}^{-1}$ (assuming 13.6 eV photon energy). The W80 bubble radius is ~ 20 pc, much larger than the Strömgren radius of ~ 2.8 pc (assuming a mean gas number density n of 100 cm^{-3} before ionization, see equation 7.24 in Krumholz 2017). Hence, the bubble has likely expanded significantly. Assuming a temperature of 10^4 K for the HII region, the corresponding sound speed is $\sim 11 \text{ km s}^{-1}$. If we assume a mean stellar mass of $0.5 M_\odot$ (Evans et al. 2009) for the Pelican cluster members, then the total cluster mass (with 247 members, R11) is $\sim 120 M_\odot$. Assuming a star formation efficiency of 3% (Kennicutt & Evans 2012), the total pre-Pelican cloud mass M would be $4 \times 10^3 M_\odot$,

First, we consider that the pre-Pelican cloud was pushed by the bubble expansion. Assuming the thermal pressure in the bubble dominates the expansion, then the total expansion time can be computed following equation 7.32 in Krumholz (2017).

$$r_i = 9.4 S_{49}^{1/7} n_2^{-2/7} T_{i,4}^{2/7} t_6^{4/7} \text{ pc}, \quad (1)$$

where r_i is the radius of the ionized sphere, S_{49} is the ionizing photon flux (in units of 10^{49} s^{-1}), n_2 is the initial number density before ionization (in units of 100 cm^{-3}), $T_{i,4}$ is the temperature of the ionized gas (in units of 10^4 K), and t_6 is the time of expansion (in units of 10^6 yr). Adopting $r_i = 20$ pc, $S_{49} = 1$, $n_2 = 1$, and $T_{i,4} = 1$, the total expansion time t is about 3.7 Myr. Taking the time derivative of the equation, the current bubble expansion velocity is

$$\frac{dr_i}{dt} = 5.4 \times t_6^{-3/7} \text{ km s}^{-1}, \quad (2)$$

which is about 3 km s^{-1} . The typical relative velocity between the molecular filaments in the NAN region and the W80 bubble is a few km s^{-1} . So the bubble expansion is a possible mechanism of dispersing the pre-Pelican cloud. Considering the geometry, it is possible that the molecular gas to the north-west of the Pelican Head is made in part from gas from the pre-Pelican cloud that has been pushed to that position.

Second, we consider that the Lyman-alpha photons from the HII region exert a radiation pressure on the molecular gas. Assuming the solid angle subtended by the pre-Pelican cloud (as viewed from the Bajamar Star) is Ω , the force caused by the radiation pressure

is $S\Omega/4\pi c$, where c is the speed of light. The final velocity of the pre-Pelican cloud after t is $(S\Omega/4\pi c)t/M$. If we assume $\Omega = 4\pi/10$, the pre-Pelican cloud reaches about 1.1 km s^{-1} , smaller than the velocity driven by the bubble expansion.

Finally, we consider that the pre-Pelican cloud was ionized by the Bajamar Star so that we do not see the molecular gas today. For an ideal Strömngren sphere, the ionized gas mass is $S_{UV}\mu m_H/n\alpha_B$, where $\mu = 1.4$ is the mean particle weight, m_H is the hydrogen mass, n is the particle density which we assumed as 100 cm^{-3} earlier (see equation 7.23 in Krumholz 2017), $\alpha_B = 3.5 \times 10^{-13} \text{ cm}^3 \text{ s}^{-1}$ is the case B recombination coefficient for hydrogen. Given the aforementioned flux S_{UV} , the HII region mass is about $3 \times 10^3 M_\odot$, comparable to the pre-Pelican cloud mass M .

The actual history of the cloud dispersal may be due to a combination of the bubble expansion, radiative pressure, and ionization. In other words, part of the pre-Pelican cloud have been ionized and the rest could have been pushed away. In any case, it is possible that the Bajamar Star and the W80 bubble together could have dispersed the pre-Pelican cloud.

5.2. The Gulf Cluster

The Gulf cluster, however, needs a closer examination. There are probably three sub-clusters in this region. From west to east, Guieu et al. (2009, hereafter G09) named them clusters 1, 2, 3 (see their figure 9). From our combined molecular line data, we find evidence that the three sub-clusters are probably separated.

In Figure 17, we show the ^{13}CO gas associated with the three G09 sub-clusters. In panel (c), the G09 cluster 3 is associated with a $24\mu\text{m}$ dark region at the northeast end of the Gulf region (the ‘‘Dark Crab’’). It is embedded in highly extinguished molecular gas at $\sim 4.9 \text{ km s}^{-1}$. Meanwhile, the G09 cluster 2 spatially matches the $24\mu\text{m}$ dark region which is the F-6 filament at a velocity of $\sim 1.5 \text{ km s}^{-1}$. Consequently, the two G09 clusters are associated with two distinct molecular gas regions. They are likely not part of the same cluster.

More interestingly, the location of the G09 cluster 1 has no $24\mu\text{m}$ dark counterpart, as can be seen in Figure 17 (b)(c). This cluster nicely coincides with the location of the background F-7 filament (Figures 11 and B8). This is especially true at 7.1 km s^{-1} (panel d). It is possible that the G09 cluster 1 is embedded in F-7, which lies on the far side of W80. There are six members in the cluster 1 with Gaia DR2 data, and their distances are (in ascending order) 1103, 1111, 1611, 1863, 2457, and 3565 pc. These distances are significantly larger than the estimated distance to W80, and thus consis-

tent with the scenario that this is a cluster background to W80.

Overall, we see that at least part of the star formation activities in the NAP complex are strongly impacted by the feedback from the Bajamar Star.

6. SUMMARY AND CONCLUSION

We present high-resolution CARMA molecular line data toward the North America and Pelican Nebulae. The new interferometer data is combined with existing single-dish data from the DLH14 telescope to study the structure and kinematics of the molecular gas in this region. The combined maps show ongoing interaction between the molecular gas and feedback from the massive Bajamar Star (O3.5) that is responsible for the W80 HII region. The molecular gas is being dispersed by W80.

The high-resolution data reveal the intricate morphology of the gas. A substantial fraction of the clouds have a very clumpy structure with sharp edges. Some of these bright edges coincide with the location of the bright infrared rims which generally point toward the Bajamar Star. We argue that they are heated by the massive star and the gas is being dispersed.

Using multi-wavelength data (optical, infrared, and millimeter), we have identified a number of distinct structures in the cloud complex, including a number of dark clouds and globules. We have cross-matched the structures in images at different wavelengths, and determined the relative line-of-sight distances of the molecular filaments and clumps.

We find that there are two groups of molecular clouds between the W80 bubble and us. The first group (‘‘gray regions’’ in the optical image) contains most of the molecular gas in the region, stretching from the Gulf region in the south to the PelHat region in the north. It is also the main host of the young stellar objects in the Nebulae. However, this group of molecular clouds is being impacted by, and will soon be dispersed, by the massive star feedback. The second group of molecular gas (‘‘dark regions’’ in the optical image) consists of scattered molecular gas clumps that are less massive. The clumps appear darker in the optical image, indicative of higher extinction towards these clumps. They show limited star formation (except for one clump we call the Dark Crab). They are being approached by the expanding W80 bubble.

To determine the distance to the NAP complex, we obtained the Gaia distances to stars in three young stellar object clusters identified by Rebull et al. (2011). The results show that the majority of the cluster members are located at $\sim 800 \text{ pc}$, indicating that the NAP complex is at this distance. We provide an interactive distance map

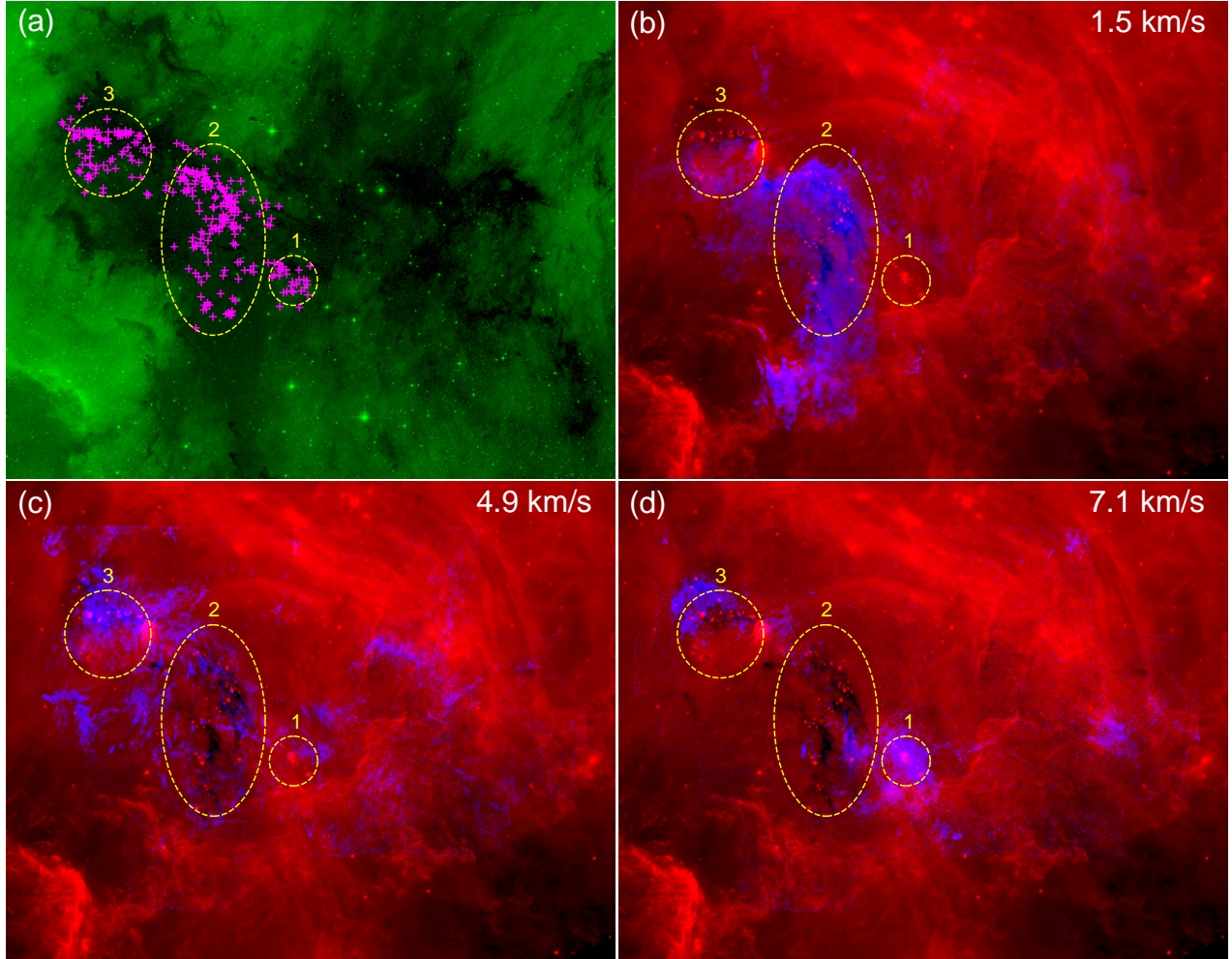


Figure 17. (a): POSS-II red color plate for the Gulf region, same as Figures B2-B8. The magenta crosses mark the R11 Gulf cluster members. The yellow dashed ellipses mark the G09 sub-clusters. (b): The background red color shows the Spitzer $24\mu\text{m}$ image from R11. The blue color shows the CARMA+DLH14 combined ^{13}CO channel map at 1.5 km s^{-1} . The $24\mu\text{m}$ dark regions are partially covered by the blue color. Readers can see them better in Figure 5. (c): Same as panel (b) but showing the 4.9 km s^{-1} channel. (d): Same as panel (b) but showing the 7.1 km s^{-1} channel.

based on the method developed in Zucker et al. (2019, 2020). The map is consistent with the $\sim 800\text{ pc}$ NAP distance, and it gives more details on the 3D structures of the complex, which is broadly consistent with our conclusions based on matching the morphology of structures seen in optical, infrared, and millimeter molecular line maps of the region.

The PelHat and Gulf clusters defined by Rebull et al. (2011) show a clear association with molecular gas. The third cluster, the Pelican cluster, is associated with substantially less molecular gas. We suggest the gas in this cluster has been dispersed by the O-type Bajamar Star, not by sources in the Pelican cluster. It seems, therefore that the star formation in the Pelican cluster has been interrupted by the massive star. The pre-Pelican cloud was probably dispersed by a combination of bubble ex-

pansion, radiative pressure, and gas ionization. This scenario provides a good example of feedback-regulated star formation. The North America and Pelican Nebulae thus provide a close-by example for studying star formation under the influence of an isolated massive star.

ACKNOWLEDGMENTS

We thank the anonymous referee for a thorough check on the paper and helpful comments. We thank Luisa Rebull for providing the Spitzer images. We thank Laurent Cambr esy for providing the extinction maps. SK acknowledges fruitful discussions with Min Fang and Serena Kim. SS acknowledges support from the European Research Council under the Horizon 2020 Framework Program via the ERC Consolidator Grant CSF-648505. TGSP gratefully acknowledges support by the National Science Foundation under grant No. AST-2009842. SK and HGA were (partially) funded by the National Science Foundation, award AST-1140063, which also provided partial support for CARMA operations. CARMA operations were also supported by the California Institute of Technology, the University of California-Berkeley, the University of Illinois at Urbana-Champaign, the University of Maryland College Park, and the University of Chicago. ASM and VO carried out this research within the Collaborative Research Centre 956 (subprojects A6 and C1), funded by the Deutsche Forschungsgemeinschaft (DFG) - project ID 184018867. Part of this research was carried out at the Jet Propulsion Laboratory, California Institute of Technology, under a contract with the National Aeronautics and Space Administration. SZ acknowledges a funding from the National Natural Science Foundation of China through grants NSF 11803091. RJS acknowledges funding from an STFC ERF (grant ST/N00485X/1). RSK acknowledges support from the Deutsche Forschungsgemeinschaft (DFG) via the Collaborative Research Center (SFB 881, Project-ID 138713538) “The Milky Way System” (sub-projects A1, B1, B2 and B8) and from the Heidelberg cluster of excellence (EXC 2181 - 390900948) “STRUCTURES: A unifying approach to emergent phenomena in the physical world, mathematics, and complex dat”, funded by the German Excellence Strategy. He also thanks for funding from the European Research Council in the ERC Synergy Grant “ECOGAL – Understanding our Galactic ecosystem: From the disk of the Milky Way to the formation sites of stars and planets” (project ID 855130).

This research made use of the data from the Milky Way Imaging Scroll Painting (MWISP) project, which is a multi-line survey in $^{12}\text{CO}/^{13}\text{CO}/\text{C}^{18}\text{O}$ along the northern galactic plane with the Purple Mountain Observatory Delingha 13.7m telescope. MWISP project is supported by National Key R&D Program of China with grant no. 2017YFA0402700, and the Key Research Program of Frontier Sciences, CAS with grant no. QYZDJ-SSW-SLH047. The Second Palomar Observatory Sky

Survey (POSS-II) was made by the California Institute of Technology with funds from the National Science Foundation, the National Aeronautics and Space Administration, the National Geographic Society, the Sloan Foundation, the Samuel Oschin Foundation, and the Eastman Kodak Corporation. The Oschin Schmidt Telescope is operated by the California Institute of Technology and Palomar Observatory.

Software: Astropy (Astropy Collaboration et al. 2013), Numpy (van der Walt et al. 2011), APLpy (Robitaille & Bressert 2012), Matplotlib (Hunter 2007)

Facilities: CARMA, DLH:13.7m

APPENDIX

A. WISE IMAGE

In Figure A1, we present a WISE RGB color image as a supplement to Figure 5.

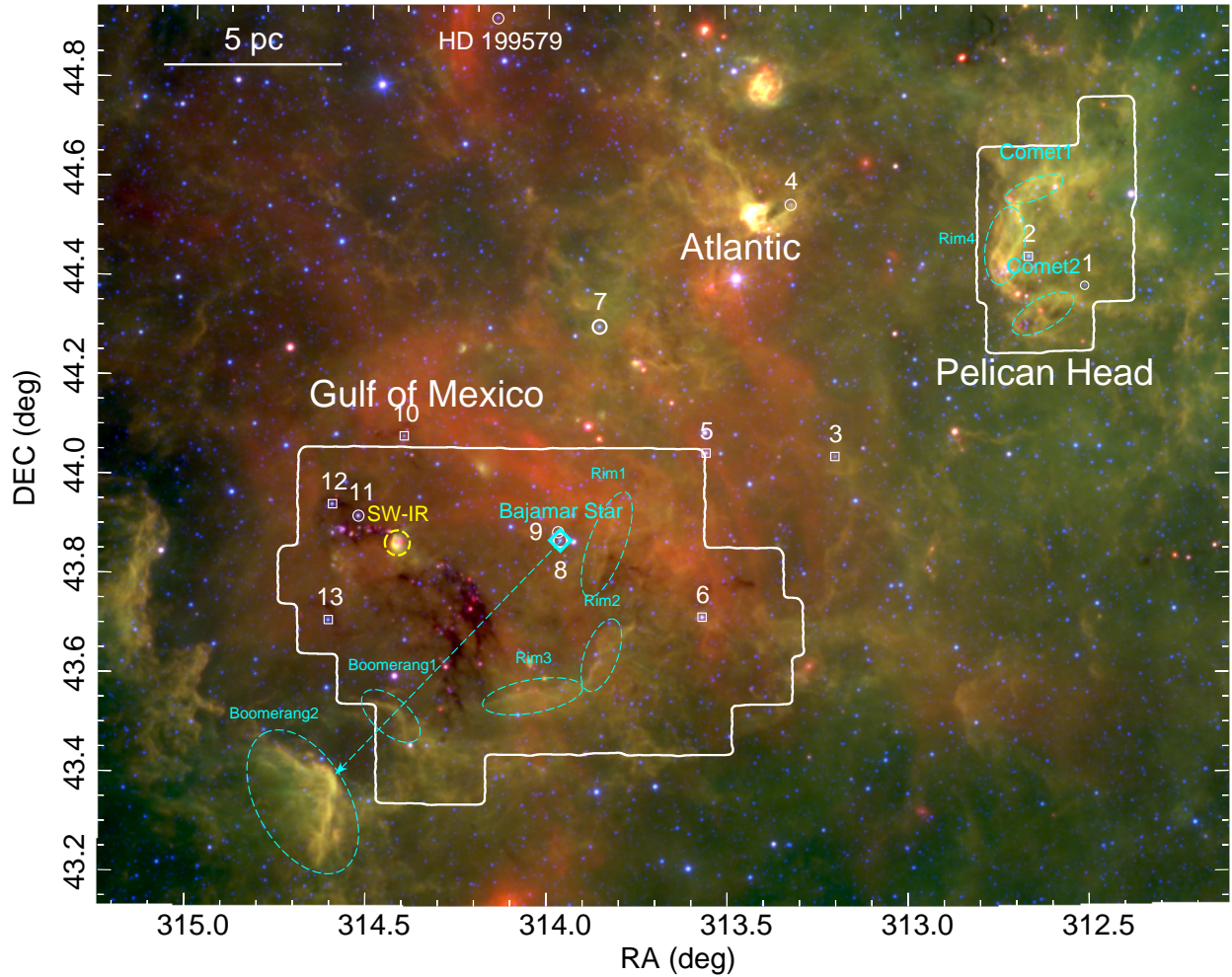


Figure A1. WISE false color RGB image using the $22\mu\text{m}$ (Red), $12\mu\text{m}$ (Green), and $4.6\mu\text{m}$ (Blue) bands. The cyan diamond marks the position of the Bajamar Star. The cyan arrow points from the Bajamar Star toward the two boomerang features at the south-east corner. The two cometary clouds are seen in molecular gas in Figure 8. The stars with numbers 1-13 are from SL08 (as shown in B14). Circles are stars classified as spectral type OB. Squares are possible AGB stars (see SL08 and B14). The Bajamar Star is #8.

B. STRUCTURE IDENTIFICATION

Figures B2-B8 show the comparison between the POSS-II red plate and the $^{13}\text{CO}(1-0)$ emission at different velocities. The seven figures have the same four-panel setup that help compare the gray/dark features in the optical images with the molecular gas distribution at large and small scales. In all panels the green colored map shows the POSS-II red plate image. Panels (a) and (b) show the large-scale NAP area (similar to the area shown in the optical and IR images in Figures 1 and 5), while panels (c) and (d) zoom in on the Gulf region. The blue color in panel (b) shows the $^{13}\text{CO}(1-0)$ emission in one channel from the DLH14-only maps. This same emission is represented with blue contour

lines in panel (a). The blue color in panel (d) shows the $^{13}\text{CO}(1-0)$ emission from the combined (CARMA+DLH14) cube at the same velocity (V_{lsr}) as the emission shown in panels (a) and (b).

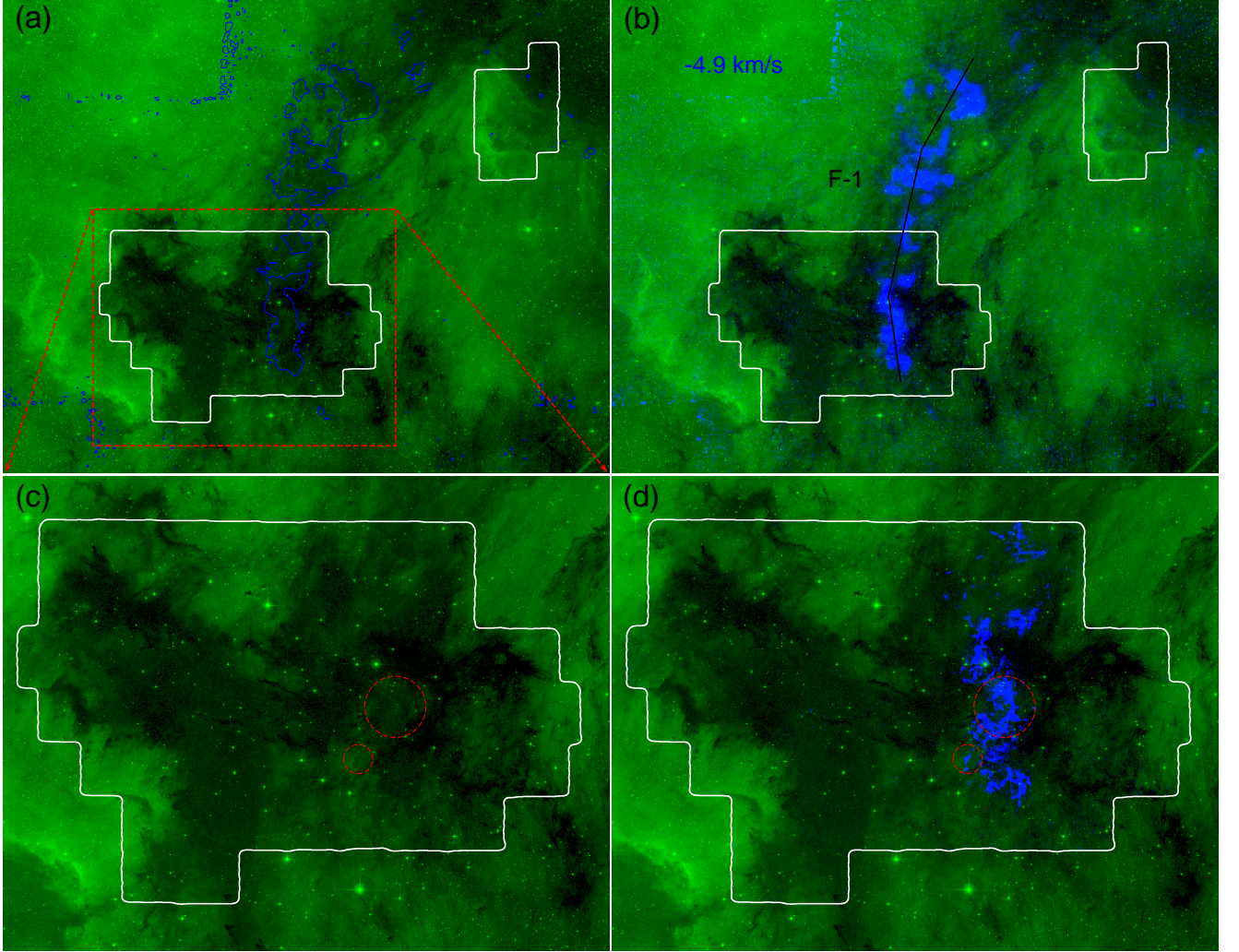


Figure B2. Comparison between the POSS-II red color ($0.7 \mu\text{m}$) and the $^{13}\text{CO}(1-0)$ cube from Z14 and the combined $^{13}\text{CO}(1-0)$ cube from this paper. **(a):** POSS-II red color plate shown in green color map. The white boundaries show the CARMA map coverage. The blue contours show the $^{13}\text{CO}(1-0)$ emission from panel (b). The red dashed box shows the zoom-in region in panel (c). **(b):** The green color and the white boundaries are the same as panel (a), but the blue color represents the $^{13}\text{CO}(1-0)$ emission from Z14. The black segment marks the F-1 filament defined in Z14. The blue text shows the channel velocity. **(c):** Zoom-in view of the red box in panel (a). **(d):** The blue color shows the $^{13}\text{CO}(1-0)$ combined (CARMA+DHL14) data from this paper. The channel velocity is the same as that in panel (b).

Figure B2 shows the distribution of the $^{13}\text{CO}(1-0)$ emission in the $V_{lsr} = -4.9 \text{ km s}^{-1}$ channel in comparison with the optical emission. At this velocity, all of the ^{13}CO emission belongs to the F-1 filament that was defined by Z14. In panel (b) we see that F-1 stretches from the Gulf to the northern Atlantic region, following the general structure of the “gray” clouds in the optical image. This is also the case at small scales, as can be seen in panel (d) (particularly see regions enclosed by the two red dashed circles). The most straightforward assumption is that the gray region is in the foreground of the W80 bubble as it shields light from the bubble. Therefore, we conclude that the F-1 filament is on the near side of the bubble, moving toward us with a V_{lsr} of $\sim -5 \text{ km s}^{-1}$.

The molecular gas in the small red circle in Figure B2 is part of the Rim2 gas that is heated by the Bajamar Star (see §3.1). In fact, both Rim1 and Rim2 are part of the southern extension of F-1, coincident with gray optical regions

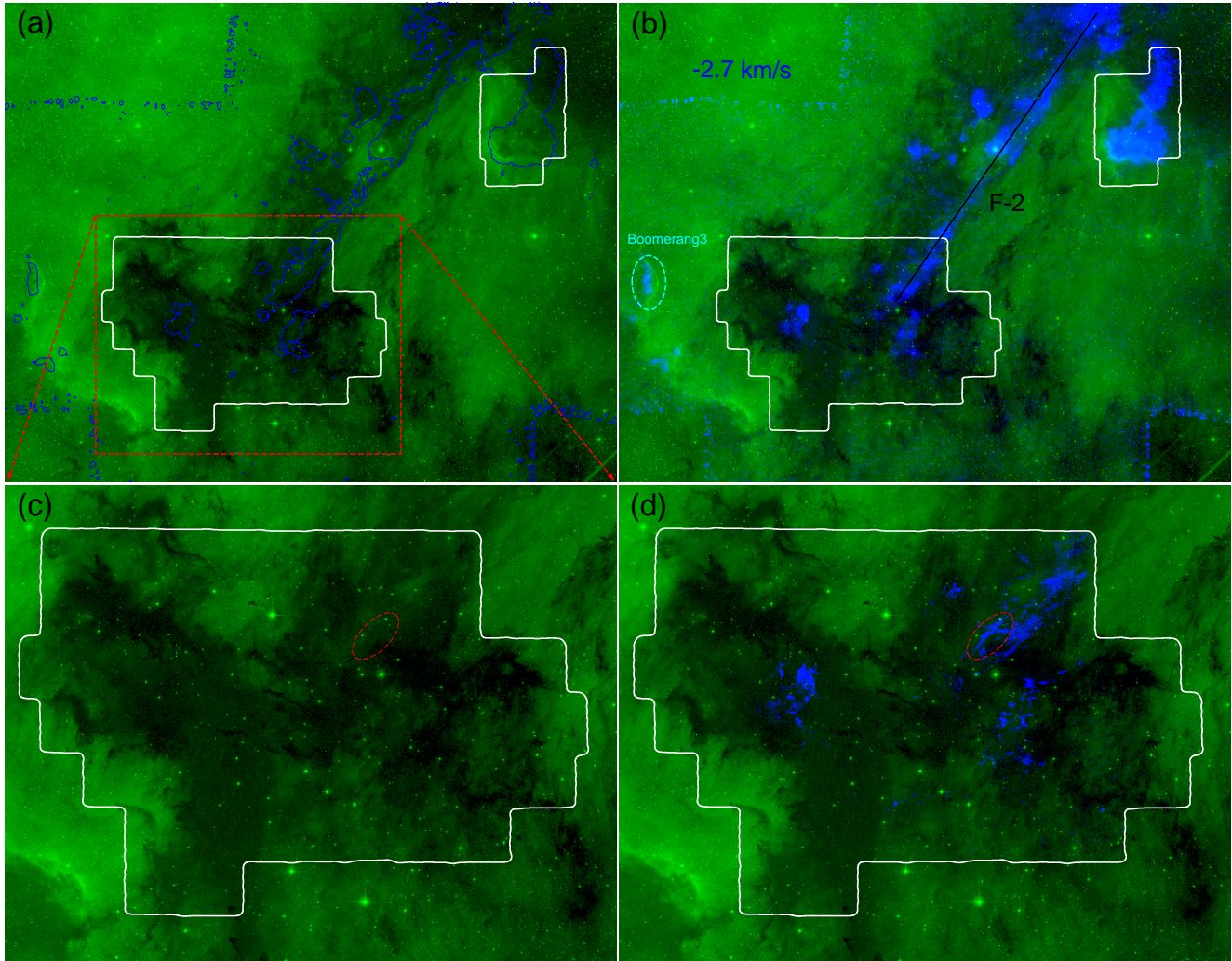


Figure B3. Same as B2, but at a velocity representative of F-2.

in the Gulf, and most prominently detected at velocities around -5 to -3 km s^{-1} , as seen in the ^{13}CO 1st-moment map (see Figure 9). Since this gas is associated with feedback features produced by radiation from the Bajamar Star, gas at these velocities likely resides not far from the HII region. Radio recombination line observations of the W80 HII region show that the V_{lsr} of this source is 5.5 ± 4.4 km s^{-1} (Lockman 1989). Given the velocity (and position) of the F-1 filament, we argue that the expanding HII region is currently exerting pressure and pushing on this filament toward us. The high excitation temperature of the gas associated with the Rim1 and Rim2 features (see Figure 6(b)) as well as the very clumpy morphology with very sharp and bright edges is evidence that the gas here is heated and sculpted by the UV radiation from the nearby high-mass star powering the HII region. Following this idea, we argue that the “gray” regions correspond to molecular gas very close to the HII region, where the gas is being dispersed by the fierce radiation from the Bajamar Star.

Figure B3 shows the distribution of the molecular gas (as traced by $^{13}\text{CO}(1-0)$) at $V_{lsr} = -2.7$ km s^{-1} . At this velocity the most prominent molecular gas feature is the F-2 filament (originally identified by Z14), which extends from the northwest edge of the map (in the northern Atlantic region), south to the central part of the Gulf region. There is clear correspondence in the morphology of the F-2 filament and the “gray” regions in the optical image, both at large scales (as traced by the DLH14 data) and at small scales (traced by the CARMA+DLH14 data). The latter is highlighted by red dashed ellipses in panels (c) and (d) of Figure B3.

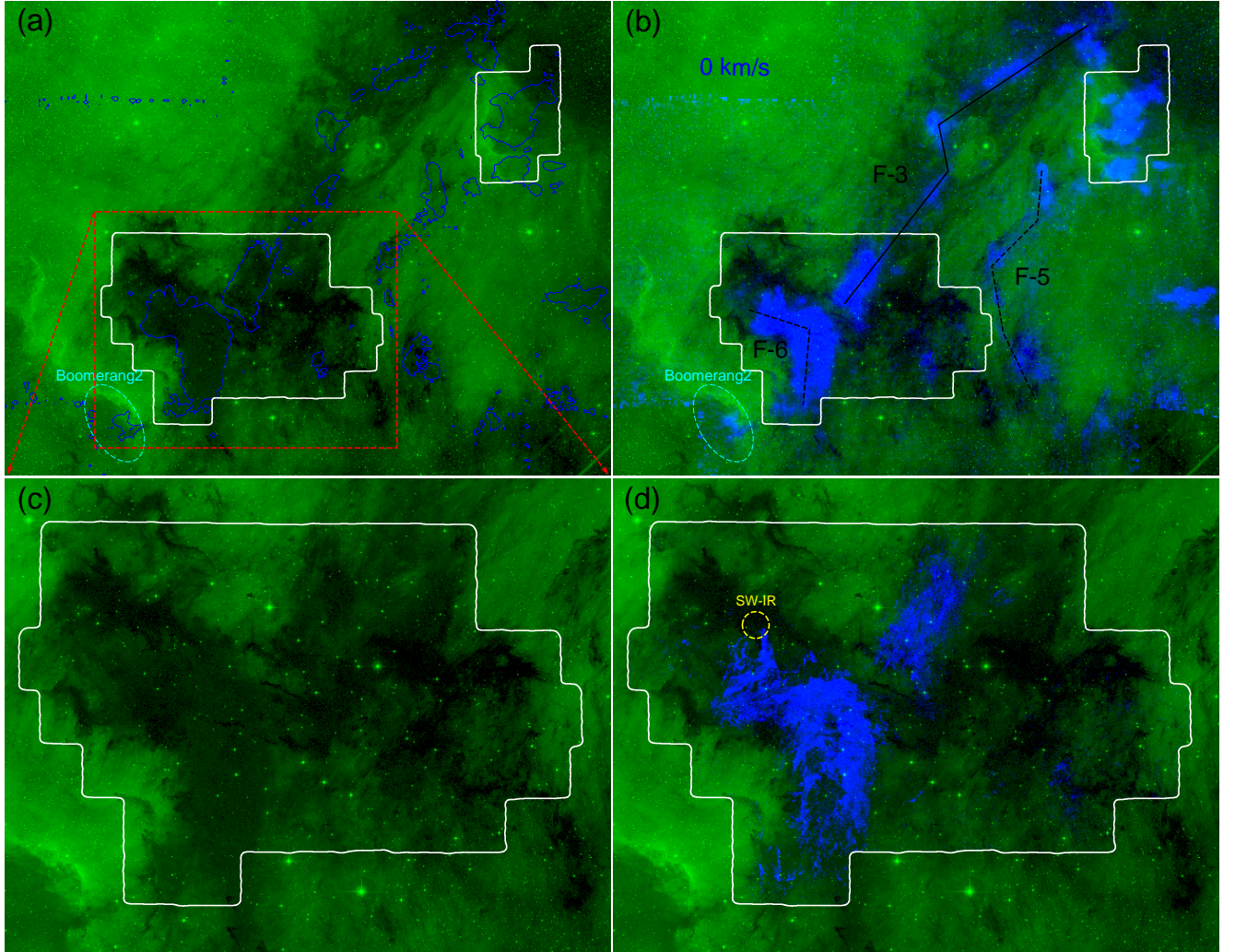


Figure B4. Same as B2, but at a velocity representative of F-3, F-5, and F-6.

Similar to F-1, the F-2 filament is in the foreground of, and has a blueshifted velocity with respect to, W80. Given the similar low extinction (i.e., being a gray region instead of a dark region in the optical image) and its close position and velocity relative to F-1, we argue that F-2 (similar to F-1) is also close to the front end of the HII region. However, since we do not see prominent bright rims or clear feedback features in F-2 as in F-1, we suspect that F-2 is farther from the bubble than F-1.

Other interesting features seen at $V_{lsr} = -2.7 \text{ km s}^{-1}$ are the gas associated with the Pelican Head bright rim region (towards the northwest) and a bright rim region in the east, which we name Boomerang3 (see Figures 11 and B3(b)). These two mark the outer regions clearly impacted by the UV radiation and the HII region within the DLH14 maps. Even though these features appear to be at (or close to) the edge of the HII region they are most likely to be foreground to W80 given there is evident (light gray) extinction next to these bright rim regions in the optical images (see Figures 1 and 11).

The above analyses of F-1 and F-2 filaments have shown that the L935 dark cloud in the NAP region is the shadow of a combination of foreground molecular filaments and clouds. The F-3 filament identified by Z14, and seen in Figure B4 at $V_{lsr} = 0 \text{ km s}^{-1}$, appears to be part of the same complex as F-1 and F-2. As shown in Figure B4, filament F-3 winds its way from the Gulf region through the Atlantic region and all the way to the northern end of the Pelican region, coincident with gray regions seen in the optical images.

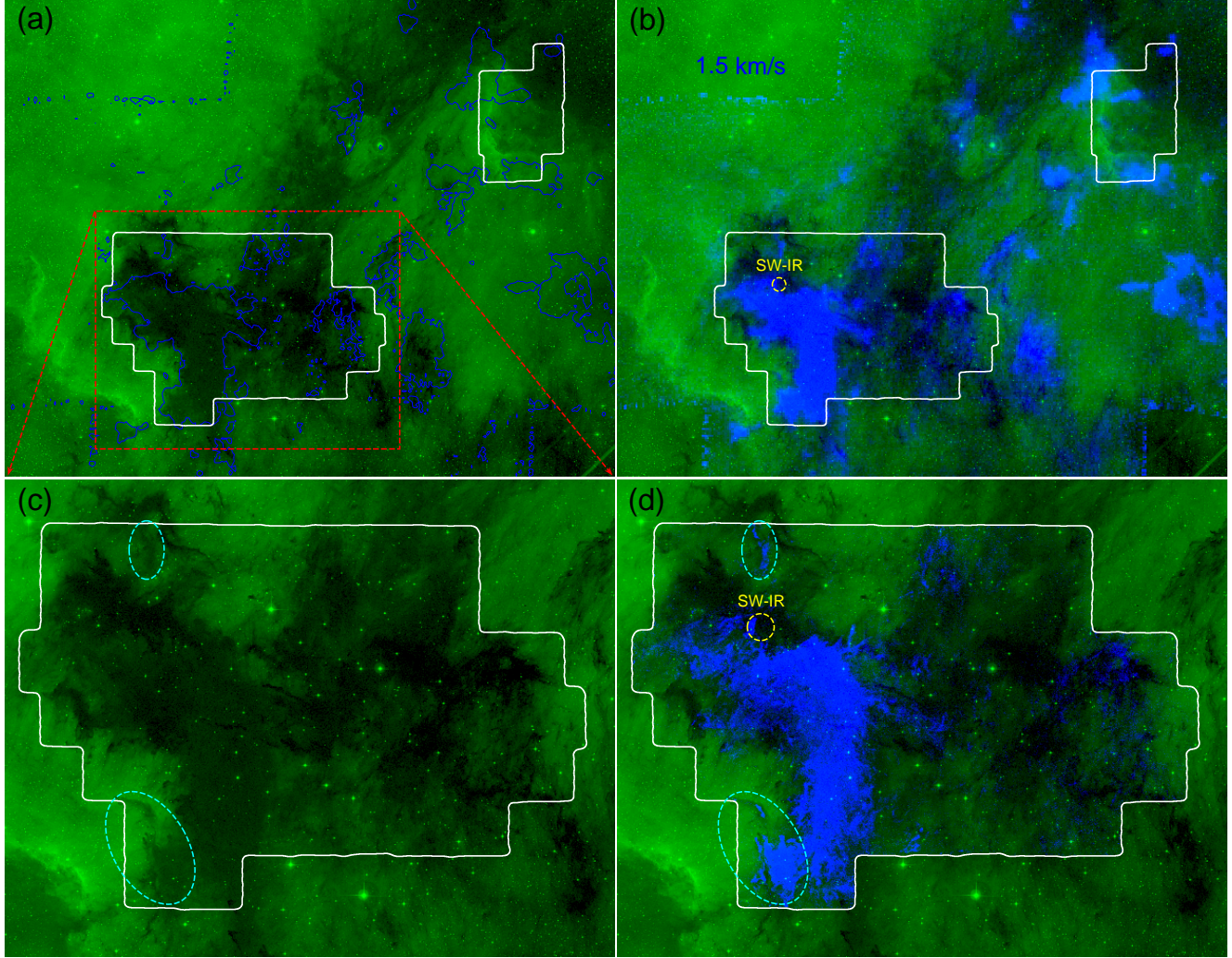


Figure B5. Same as B2, but at a velocity representative of F-6 and Boomerang1.

Two other prominent features are seen at velocities similar to those of F-3 (Figure B4). One of these is a filament lying on the west side of the L935 dark cloud that follows a grayish silhouette in the optical image, which we name F-5, following the nomenclature from Z14. The other feature is the thick filament with an “inverted L” morphology in the Gulf region. This filament, which we name F-6, corresponds to the $24\ \mu\text{m}$ dark region in Figure 5, and includes the BGPS dust continuum clumps SW1, SW2 main, SW2 SE, and SW2 S identified by B14 (which we show in Figure 6), as well as many $24\ \mu\text{m}$ sources, and 3 YSO clusters identified by R11. Figure B4 shows that the optical counterpart of F-6 is a grayish region, similar in appearance to the optical counterparts of F-1, F-2, F-3. This region is clearly in the foreground of W80, but has not (yet) been severely impacted by the massive star. Other features seen at $V_{lsr} \sim 0\ \text{km s}^{-1}$ include the CO emission associated with Boomerang2 in the southeast edge of the NAP complex, as well as parts of the Pelican region. As with similar features discussed above, these structures are most likely foreground to W80.

Figure B5 shows the comparison for molecular gas at $V_{lsr} = 1.5\ \text{km s}^{-1}$ and the optical image. At this velocity the most prominent feature is gas associated with the F-6 filament described above (also seen at $V_{lsr} = 0\ \text{km s}^{-1}$). In addition, at this velocity there are two interesting structures which show a good match between the morphology of the CO and gray extinction in the optical image. One is the Boomerang1 feature seen in Figure 11 as a gray feature (see also Figure 5), where the ^{13}CO emission nicely matches the morphology of the feedback structure. There is also a good match between the optical and the molecular gas images southwest of Boomerang1. The other structure is the silhouette highlighted by the cyan ellipse in Figure B5, at the northern edge of the Gulf region covered by our CARMA

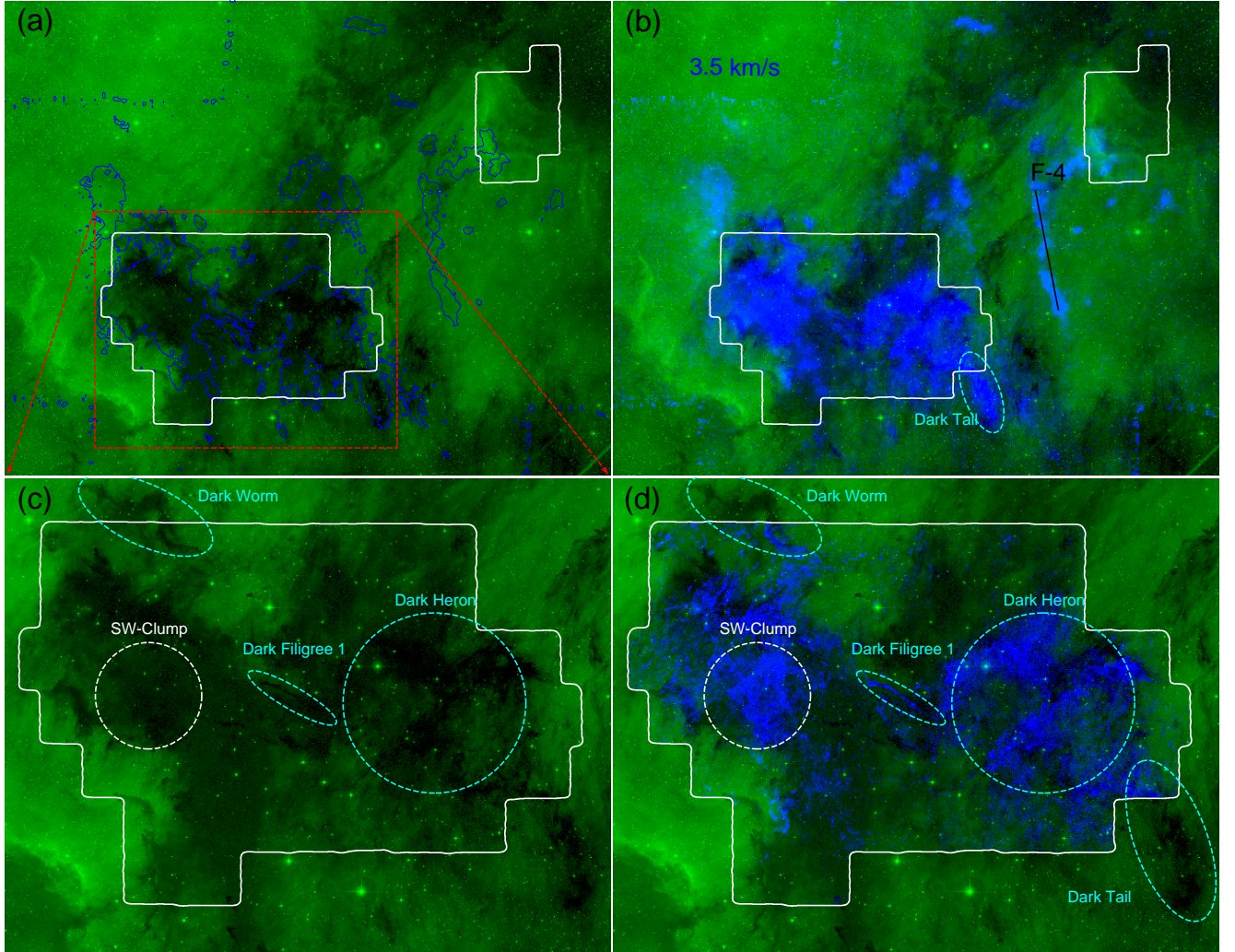


Figure B6. Same as B2, but at a velocity representative of the dark clumps.

observations. As with the other features described above, the clear correspondence between the gas morphology and gray extinction implies these features are foreground to the HII region. Since their LSR velocity is lower than the aforementioned W80 velocity ($\sim 5.5 \text{ km s}^{-1}$), they are likely moving away from the bubble.

The molecular gas counterparts of the dark extinction regions begin to appear at higher LSR velocities. Figure B6 shows the comparison for the ^{13}CO emission at $V_{lsr} = 3.5 \text{ km s}^{-1}$ and the optical image. The dark region in the Gulf region marked by the big dashed (cyan) circle (which we name “Dark Heron”) nicely matches the molecular gas structure. The structure extends beyond the southwest border of our CARMA coverage, where we see the CO emission (from the DLH14-only data) match the dark structure we name “Dark Tail”. Another intriguing structure is seen at the center of the Gulf region, highlighted by a dashed ellipse in panels (c) and (d) of Figure B6. It is a thin dark filament that is only seen in the high-resolution combined data (hereafter we name it “Dark Filigree 1”). Another dashed circle in this figure marks the structure we name the “SW-Clump”, which is to the east of the SW2 Main and SW2 SE dust continuum clumps identified by B14. This structure appears as a darker region on top of, but with a moderately distinct velocity component in ^{13}CO gas compared to, the gray F-6 filament. It is, therefore, not clear if it is part of F-6 (see §4.2). At the northeast corner of the Gulf region we see the “Dark Worm” at the border of the CARMA mosaic footprint. We see its bottom half in the combined image, which matches well the dark filament in the optical image.

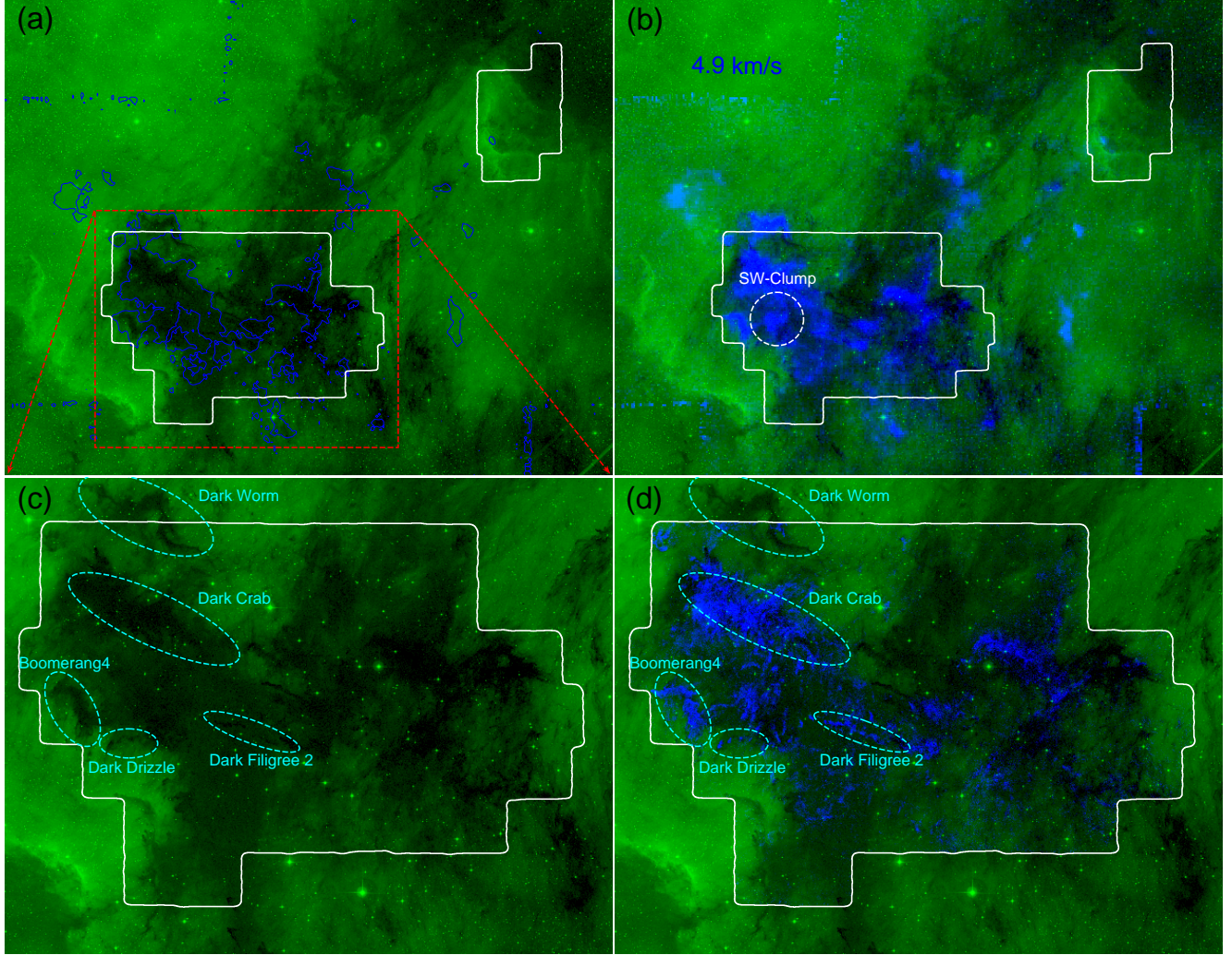


Figure B7. Same as B2, but at a velocity representative of the dark clumps.

It is evident that these dark features are foreground molecular gas, and given their LSR velocity compared to that of W80, they are moving away from the HII region. Unlike many of the structures coincident with gray extinction regions, the structures at this velocity do not show clear evidence of being impacted by feedback from the high-mass star powering the HII region. Because of this and the higher extinction we suggest that the dark regions are farther from the bubble compared to the gray regions.

At $V_{lsr} = 3.5 \text{ km s}^{-1}$ we also detect emission from the filament F-4, originally defined by Z14 (see Figure B6). This CO structure does not show any gray or dark counterpart in the optical image. Since it shows no optical extinction counterparts, the filament is very likely on the back side of the bubble. There is another clump to the northeast of the Gulf white boundary. It shows no foreground extinction. So it should also be on the far side. Its velocity roughly peaks at 4 km s^{-1} .

Figure B7 shows the comparison between the optical image and ^{13}CO emission at $V_{lsr} = 4.9 \text{ km s}^{-1}$. At this velocity, a significant fraction of the molecular gas is coincident with “dark” regions that are significantly smaller than the filaments discussed earlier, and have the appearance of scattered clumps and drizzles, shielding light from W80 in the background. We define four structures based on where the CO morphology at this velocity matches that of dark regions. These are the “Dark Crab”, “Boomerang4”, “Dark Filigree 2”, and “Dark Drizzle”. One interesting feature is that the “Dark Drizzle” and the “Dark Filigree 2” structures are broken into small dark globules, each globule having its own ^{13}CO counterpart. The typical angular size of the globules is about $10\text{--}15''$. At a distance of 800 pc (see §4.3),

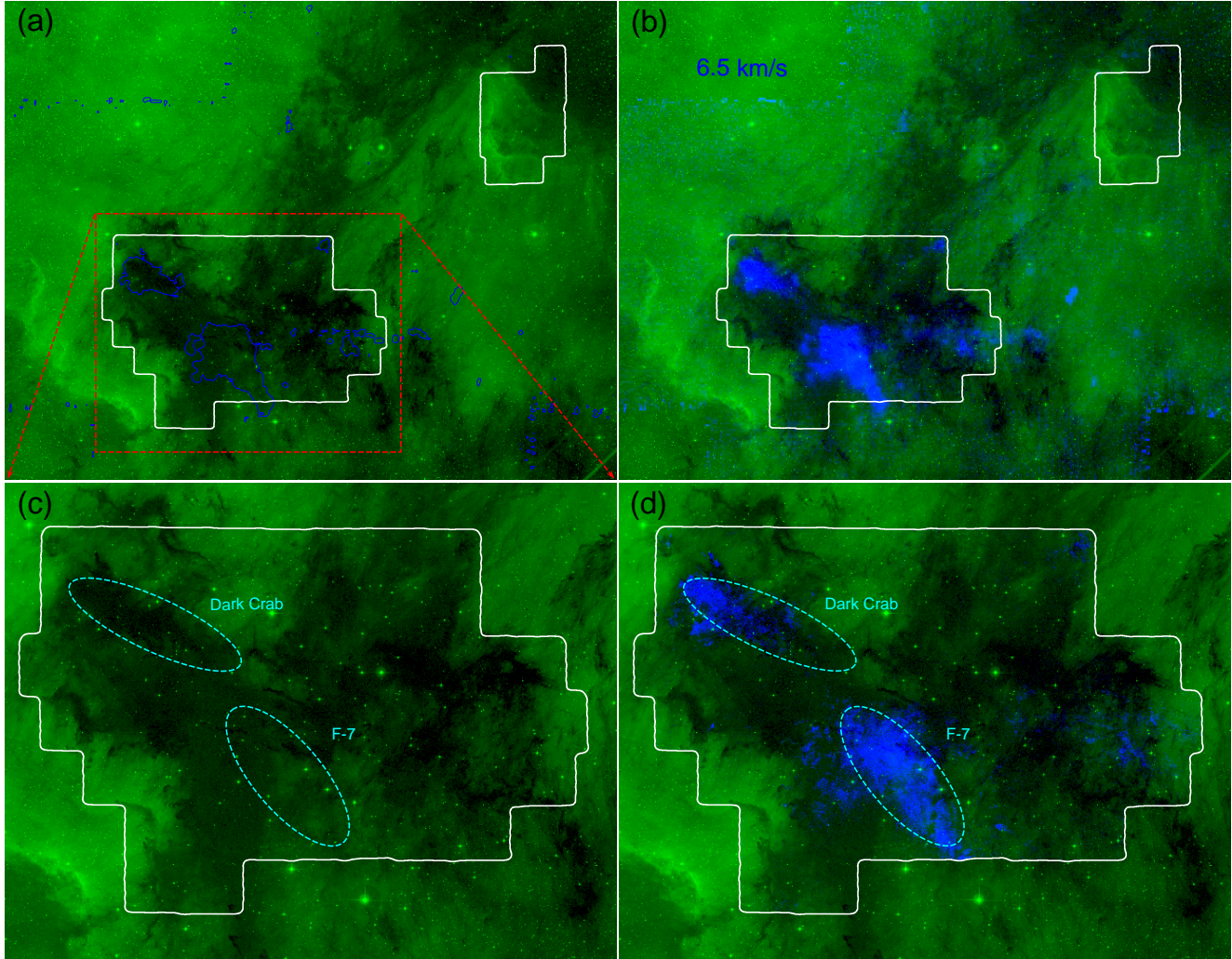


Figure B8. Same as B2, but at a velocity representative of F-7.

their physical size is $\sim 10^4$ AU, reminiscent of Bok globules (e.g., Barnard 68, Alves et al. 2001). The Dark Crab approximately coincides in position with F-6, but it is at a higher velocity. We therefore argue that the Dark Crab is in front of F-6, with a velocity similar to that of W80.

At a $V_{lsr} = 6.5$ km s $^{-1}$, there are two main structures in ^{13}CO emission (see Figure B8). One of these structures is associated with the Dark Crab, which we first identified when comparing the optical image of the Gulf region with the ^{13}CO emission at $V_{lsr} = 4.9$ km s $^{-1}$ (Figure B7). At $V_{lsr} = 6.5$ km s $^{-1}$ most of the CO emission is concentrated towards the northeast half of the Dark Crab, whereas at lower LSR velocity the emission associated with the Dark Crab covers the full extent of this dark cloud. The other structure at $V_{lsr} = 6.5$ km s $^{-1}$, which we name F-7, lies in the southern part of the Gulf region and is elongated in the northeast-southwest direction. Unlike other CO structures we identify above, the morphology of F-7 does not closely match the structure of any of gray or dark extinction features which it overlaps. We thus argue that F-7 is not responsible for any of the extinction in the region as it is on the far side of W80. Given the LSR velocity of F-7, it is likely F-7 is moving away from W80 (see §5.1 and Figure 17).

REFERENCES

- Allamandola, L. J., Tielens, A. G. G. M., & Barker, J. R. 1989, *ApJS*, 71, 733
- Alves, J. F., Lada, C. J., & Lada, E. A. 2001, *Nature*, 409, 159

- Astropy Collaboration, Robitaille, T. P., Tollerud, E. J., et al. 2013, *A&A*, 558, A33
- Bailer-Jones, C. A. L., Rybizki, J., Fouesneau, M., Mantelet, G., & Andrae, R. 2018, *AJ*, 156, 58
- Bally, J., Ginsburg, A., Probst, R., et al. 2014, *AJ*, 148, 120
- Bally, J., & Scoville, N. Z. 1980, *ApJ*, 239, 121
- Bertoldi, F. 1989, *ApJ*, 346, 735
- Cambr esy, L., Beichman, C. A., Jarrett, T. H., & Cutri, R. M. 2002, *AJ*, 123, 2559
- Churchwell, E., Povich, M. S., Allen, D., et al. 2006, *ApJ*, 649, 759
- Comer on, F., & Pasquali, A. 2005, *A&A*, 430, 541
- Dale, J. E., Haworth, T. J., & Bressert, E. 2015, *MNRAS*, 450, 1199
- Damiani, F., Pillitteri, I., & Prisinzano, L. 2017, *A&A*, 602, A115
- Evans, Neal J., I., Dunham, M. M., J orgensen, J. K., et al. 2009, *ApJS*, 181, 321
- Fang, M., Hillenbrand, L. A., Kim, J. S., et al. 2020, *ApJ*, 904, 146
- Ginsburg, A., Glenn, J., Rosolowsky, E., et al. 2013, *ApJS*, 208, 14
- Gorski, K. M., Hivon, E., Banday, A. J., et al. 2005, *The Astrophysical Journal*, 622, 759–771.
<http://dx.doi.org/10.1086/427976>
- Guieu, S., Rebull, L. M., Stauffer, J. R., et al. 2009, *ApJ*, 697, 787
- Ho, L. C., & Keto, E. 2007, *ApJ*, 658, 314
- Hunter, J. D. 2007, *Computing in Science and Engineering*, 9, 90
- Kennicutt, R. C., & Evans, N. J. 2012, *ARA&A*, 50, 531
- Koda, J., Sawada, T., Wright, M. C. H., et al. 2011, *ApJS*, 193, 19
- Kong, S., Arce, H. G., Feddersen, J. R., et al. 2018, *ApJS*, 236, 25
- Krumholz, M. R. 2017, *Star Formation*, doi:10.1142/10091
- Kuhn, M. A., & Hillenbrand, L. A. 2020, *Research Notes of the American Astronomical Society*, 4, 224
- Kuhn, M. A., Hillenbrand, L. A., Carpenter, J. M., & Avelar Menendez, A. R. 2020, *ApJ*, 899, 128
- Lockman, F. J. 1989, *ApJS*, 71, 469
- Ma ız Apell aniz, J., Sota, A., Arias, J. I., et al. 2016, *ApJS*, 224, 4
- Ossenkopf, V., Krips, M., & Stutzki, J. 2008, *A&A*, 485, 917
- Rebull, L. M., Guieu, S., Stauffer, J. R., et al. 2011, *ApJS*, 193, 25
- Reid, M. J., Menten, K. M., Brunthaler, A., et al. 2019, *ApJ*, 885, 131
- Robitaille, T., & Bressert, E. 2012, *APLpy: Astronomical Plotting Library in Python*, Astrophysics Source Code Library, , ascl:1208.017
- Straizys, V., & Laugalys, V. 2008, *Baltic Astronomy*, 17, 143
- Stutzki, J., Bensch, F., Heithausen, A., Ossenkopf, V., & Zielinsky, M. 1998, *A&A*, 336, 697
- Su, Y., Yang, J., Zhang, S., et al. 2019, *ApJS*, 240, 9
- van der Walt, S., Colbert, S. C., & Varoquaux, G. 2011, *Computing in Science & Engineering*, 13, 22.
<http://aip.scitation.org/doi/abs/10.1109/MCSE.2011.37>
- Wendker, H. 1968, *ZA*, 68, 368
- Westerhout, G. 1958, *BAN*, 14, 215
- Zhang, S., Xu, Y., & Yang, J. 2014, *AJ*, 147, 46
- Zhang, S., Yang, J., Xu, Y., et al. 2020, *ApJS*, 248, 15
- Zucker, C., Speagle, J. S., Schlafly, E. F., et al. 2020, *A&A*, 633, A51
- . 2019, *ApJ*, 879, 125